

Master Thesis



Czech
Technical
University
in Prague

F4

Faculty of Nuclear Sciences and Physical Engineering
Department of Physics

Suprathermal electron diagnostics for the COMPASS tokamak using EC emission

Bc. Michal Farník

Supervisor: Ing. Jakub Urban, Ph.D.

Field of study: Physics and Thermonuclear Fusion Technology

May 2018



Katedra: fyziky

Akademický rok: 2017/18

ZADÁNÍ DIPLOMOVÉ PRÁCE

Student: Bc. Michal Farník

Studijní program: Aplikace přírodních věd

Obor: Fyzika a technika termojaderné fúze

Název práce: Diagnostika supratermálních elektronů na tokamaku COMPASS
(česky) pomocí EC emise

Název práce: Suprathermal electron diagnostics for the COMPASS tokamak using
(anglicky) EC emission

Pokyny pro vypracování:

1. Popsat teorii a současný stav poznání ubíhajících elektronů v tokamacích.
2. Nastudovat metody pro mikrovlnnou diagnostiku elektronové cyklotronní emise.
3. Seznámit se důkladně s technikou mikrovlnného radiometru pro tokamak COMPASS.
4. Simulovat šíření a emisi elektronových cyklotronových vln v tokamaku COMPASS v přítomnosti supratermálních elektronů.
5. Navrhnout a uskutečnit experimenty na tokamaku COMPASS, které umožní studium ubíhajících elektronů. Během experimentů detekovat elektronovou cyklotronní emisi pomocí mikrovlnného radiometru.
6. Vhodnými metodami zpracovat data z uskutečněných experimentů.
7. Na základě simulací a experimentálních dat studovat jevy spojené s ubíhajícími elektrony. Zaměřit se například na primární generaci nebo udržení ve flat-top fázi výboje.

Doporučená literatura:

1. J. Wesson and D.J. Campbell: Tokamaks, 2004
2. I. H. Hutchinson: Principles of Plasma Diagnostics, 2nd ed., 2002
3. K. Kato, I. H. Hutchinson: Nonthermal electron velocity distribution measured by electron cyclotron emission in Alcator C tokamak. Physical Review Letters, 56, 340 (1986)
4. W. W. Eshetua et al.: Vertical electron cyclotron emission diagnostic for TCV plasmas, EPJ Web of Conferences, 03011 (2012)
5. O. Ficker et al.: Losses of runaway electrons in MHD-active plasmas of the COMPASS tokamak, Nucl. Fusion 57, 076002 (2017)
6. R. S. Granetz et al.: An ITPA joint experiment to study runaway electron generation and suppression a, Physics of Plasmas, 21, 072506 (2014)

Jméno a pracoviště vedoucího diplomové práce:

Ing. Jakub Urban, Ph.D.
Ústav fyziky plazmatu AV ČR, v.v.i.
Za Slovankou 1782/3
182 00 Praha 8

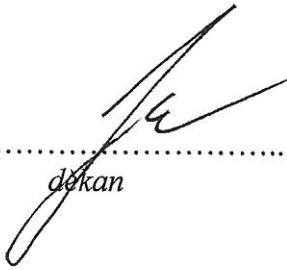
Datum zadání diplomové práce: 20.10.2017

Termín odevzdání diplomové práce: 07.05.2018

Doba platnosti zadání je dva roky od data zadání.


.....
vedoucí katedry




.....
dekan

V Praze dne 20.10.2017

Acknowledgements

I would like to thank my supervisor Ing. Jakub Urban, Ph.D. for helpful suggestions and discussions about simulations and a data interpretation; the RE electron team (O. Ficker, E. Macúšová, J. Mlynář etc.) for many valuable advices about RE physics and their dedication to the topic, microwave diagnostic team (J. Zajac, O. Bogár and M. Varavin) for help with the experimental setup of the radiometer; operators for the long stands during the RE campaigns; the whole COMPASS team for maintaining the tokamak properly functioning and last but not least I would like to thank my family and my girlfriend who supported me throughout the whole study.

This work was supported by the Czech Science Foundation Project No. GA18-02482S.

Prohlášení

Prohlašuji, že jsem svou bakalářskou práci vypracoval samostatně a použil jsem pouze podklady uvedené v příloženém seznamu. Nemám závažný důvod proti použití tohoto díla ve smyslu §60 zákona č.121/2000 Sb., o právu autorském, o právech souvisejících s právem autorským a o změně některých zákonů (autorský zákon).

V Praze, 7. května 2018

Abstract

This thesis deals with electron cyclotron emission diagnostics of runaway electrons in the COMPASS tokamak. The goal was to utilize the final design of the radiometer for the runaway electron measurements with the help of simulations. This diagnostics uses the vertical view of a plasma along the line of the constant magnetic field and receives the waves with the frequencies 76.5–88.3 GHz. In this setup it is able to measure the low-energy runaway electrons with the energies 50–140 keV. Due to the COMPASS tokamak parameters we have to take into account the detection of a reflected emission. The measurements proved the absence of a spurious signal and unfavourable dependences on the electron density and temperature. It was determined that the runaway electrons are the signal source and it is able to measure their primary generation very well. The EC wave measurement proved to be useful tool for the runaway electron research and it can be used as a standard diagnostics for the following experiments.

Keywords: tokamak, plasma, electron cyclotron emission, runaway electrons, radiometer, diagnostics

Supervisor: Ing. Jakub Urban, Ph.D.
Ústav fyziky plazmatu,
Za Slovankou 1782/3,
182 00 Praha 8

Abstrakt

Tato práce se zabývá diagnostikou elektronové cyklotronové emise ubíhajících elektronů na tokamaku COMPASS. Cílem bylo na základě simulací navrhnout finální design radiometru pro měření ubíhajících elektronů. Tato diagnostika používá vertikální pohled podél siločáry konstantního magnetického pole a přijímá vlny s frekvencemi 76,5–88,3 GHz. V tomto zapojení lze měřit nízkoenergetické ubíhající elektrony s energiemi 50–140 keV. Díky parametrům tokamaku COMPASS musíme při analýze počítat s detekcí odraženého záření. Měření potvrdila absenci parazitního signálu i nežádoucích závislostí na elektronové hustotě a teplotě. Bylo potvrzeno, že detekovaný signál pochází z ubíhajících elektronů a dokáže výborně měřit jejich primární generaci. Měření EC vln se prokázalo jako účinný nástroj pro zkoumání ubíhajících elektronů a může být použito jako standardní diagnostika v rámci dalších experimentů.

Klíčová slova: tokamak, plasma, elektronová cyklotronová emise, ubíhající elektrony, radiometr, diagnostika

Překlad názvu: Diagnostika suprathermálních elektronů na tokamaku COMPASS pomocí EC emise

Contents

Introduction	1	6.6 Other RE Experiments	64
Part I		6.6.1 Massive Gas Injection Experiments	64
Theoretical Background		6.6.2 Resonant Magnetic Perturbations Experiments	66
1 Tokamak Plasma	7	Conclusions	69
1.1 Plasma	7	Index	73
1.2 Tokamak	8	Bibliography	75
2 Runaway Electrons	13		
2.1 Runaway Electron Generation . .	14		
2.1.1 Dreicer Mechanism	14		
2.1.2 Hot-tail Mechanism	16		
2.1.3 Secondary Mechanism	17		
2.2 Runaway Electron Diagnostics . .	18		
3 Waves in Plasma	23		
3.1 Plasma Oscillations	24		
3.2 Waves in Unmagnetized Plasma	25		
3.3 Waves in Cold Magnetized Plasma	26		
3.3.1 Dielectric Tensor	26		
3.3.2 Dispersion Relation	27		
3.3.3 Polarizations	29		
3.3.4 Cutoffs and Resonances	30		
3.4 Waves in Hot Plasma	30		
3.5 Electron Cyclotron Waves	32		
3.5.1 Suprathermal ECE	33		
3.6 Ray Tracing	34		
3.6.1 SPECE Code	37		
Part II			
Experimental Setup and Results			
4 Experimental Setup	41		
4.1 COMPASS Tokamak	41		
4.2 ECE/EBW Heterodyne Radiometer	42		
5 Simulations and Calculations	45		
5.1 Frequency Range and Energy Spectra	45		
5.2 Optical Depth	47		
6 Measurements and Data Analysis	53		
6.1 Discharge Characteristics	54		
6.2 Emission Source Verification . . .	55		
6.3 O-mode/X-mode Comparison . .	58		
6.4 High B discharges	59		
6.5 Primary Generation Measurements	60		



Introduction

Demand for the energy is rising worldwide. This fact is caused by the industrialisation and everyday life simplification efforts. Nowadays the main energy source are fossil fuels. According to their exhaustion and increasing drilling and extraction, it is necessary to find some new stable sources. Renewable sources such as biomass, water, wind and solar power plants come into consideration. Nevertheless, these sources are not sufficiently steady and have to deal with a considerably high ecological load during their construction and liquidation. Another possibility could be an improvement of the present state nuclear fission power plants. The problem with fission power plants consists in the quite low public approval rating and the fear from an accident and the nuclear waste production. Nuclear fusion power plant can be one of the solutions.

Scientists research the nuclear fusion reaction for the energy gain since the discovery in 40's. The difference in the mass between the reactants in the form of light nuclei and products in the form of heavier nuclei and subatomic particles makes it possible. For example, the Sun and every other star exploit the process in their cores. On smaller scales, it is much more complicated due to the probability of the reaction. The light nuclei need to overcome the Coulomb barrier of the other atom. Owing to this problem, thermonuclear fusion, where the reactants gain the energy from a thermal movement, seems to be the most promising way to build a fusion reactor.

The fusion reaction is possible in a matter with temperatures of hundreds of millions Kelvins. In this terms the matter occurs in the state of a plasma. One of the methods to create and sustain a plasma is by using a contorted magnetic field. The most developed approach on the road to a future nuclear fusion power plant is a device called tokamak. Tokamak uses a helical magnetic field to confine a plasma in a toroidally shaped vacuum chamber. Stable and long-term fusion confinement is struggling with many problems of plasma behaviour. The understanding of the high temperature plasma phenomena precludes us to develop a controlled and economically favourable fusion. This is the reason why it is necessary to explore sufficiently accurate plasma diagnostic methods, which could help us to observe and describe a problematic plasma behaviour. We use probes, beams, spectroscopic, magnetic and wave diagnostics. Wave diagnostics excels in the accuracy and continuous output.

Active methods emit electromagnetic waves into the plasma and analyse the reflections or propagation. Passive diagnostics measure the waves emitted by the plasma itself. One of them is a electron cyclotron emission (ECE) measurement which is the subject of this thesis

Magnetic field confinement researchers look up to the crucial project called International Thermonuclear Experimental Reactor, ITER. Its task is to confine a plasma for tens of minutes and to achieve sustained deuterium-tritium plasma. Main goal is to reach the break-even and further fusion energy should overcome the energy supplied by the additional heating systems by the factor of ten ($Q = 1$). However, sudden terminations of confined plasma called disruptions present a serious threat to this device. A lot of efforts are focused on the disruption mitigation technologies, together with proper early warning diagnostic methods. Disruption event can induce so called runaway electrons (RE). Beam of such fast relativistic electrons presents one of the most dangerous issues to the tokamak first wall, thus the RE experiments are performed in many tokamaks including the COMPASS tokamak operated at Institute of Plasma Physics of the Czech Academy of Sciences in Prague. This thesis deals with the low-energy runaway electron diagnostics using electron cyclotron emission.

This thesis will be split in two parts: Part I will describe the theoretical background for the performed measurements. Part II will focus on the experimental setup, simulations and measurements and their subsequent analysis. In chapter 1 a tokamak and plasma will be introduced and defined together with important terminology and topology. The runaway electron physics, generation mechanisms and detection methods will be presented in chapter 2. Detailed look at waves in plasma with the derivations of dispersion relations will be provided in chapter 3. In this chapter cutoff and resonance conditions and principally the electron cyclotron emission phenomenon will be highlighted. At the end of this chapter there will be a brief introduction of a ray-tracing, especially the SPECE code used in the design of the diagnostics and data analysis. Part II will start with a description of the COMPASS tokamak and used heterodyne radiometer in chapter 4. The simulations and calculations in chapter 5 which helped to the final design of the diagnostics will be presented. Finally, in chapter 6 the validation of the electron cyclotron emission source will be provided. Then the measurements of the electron cyclotron emission from the low-energy runaway electrons and their subsequent analysis will be presented.



Part I

Theoretical Background

Chapter 1

Tokamak Plasma

Tokamak is currently the most developed magnetic confinement system and represents a possible way to future fusion reactors. All the experiments described in this thesis were performed in a tokamak device. This chapter describes the important terminology and quantities used throughout the thesis and provides an introduction to the tokamak plasma physics.

First, the plasma definition and principal formulas are presented in section 1.1. Then the description of a tokamak device is provided together with a basic tokamak topology and coordinate systems in section 1.2.

1.1 Plasma

Plasma is a quasi-neutral system of charged and neutral particles that behave collectively. [1]

By the quasi-neutrality we mean the fact that a macroscopic volume seems to be neutral, even though it contains a significant number of charged particles. Plasma has this attribute when its characteristic length L is larger than the Debye length λ_D , which is the distance where the electric potential of an inserted charged particle is shielded at $1/e$ of its original value. The important characteristic lengths of a plasma in an external magnetic field B are

$$\lambda_D^2 = \frac{\varepsilon_0 k_B}{\sum_{\alpha} Q_{\alpha}^2 n_{\alpha} / T_{\alpha}} \quad \text{and} \quad r_{L\alpha} = \frac{m_{\alpha} v_{\perp}}{Q_{\alpha} B} \quad (1.1)$$

which correspond to the Debye length and the Larmor radius of the cyclic motion of an α -type plasma particle with the perpendicular velocity v_{\perp} around the magnetic field line. The quantity m_{α} represents the mass of the particle, Q_{α} its charge, n_{α} the density, T_{α} the temperature, ε_0 the vacuum permittivity and k_B is the Boltzmann constant.

If the Coulomb interaction between charged particles has a longer range than the binary collision effects, we talk about the collective behaviour of plasma. System change due to the collisions is characterised by the collision frequency ν . This is the reciprocal value of the mean time when a particle loses its momentum in the original movement direction. The important

characteristic frequencies of a plasma in an external magnetic field are

$$\omega_{p\alpha} = \sqrt{\frac{n_\alpha Q_\alpha^2}{m_\alpha \varepsilon_0}}, \quad \nu_{\alpha\beta} = n_\beta \frac{Q_\alpha^2 Q_\beta^2}{(4\pi\varepsilon_0)^2 v^3} \frac{4\pi(m_\alpha + m_\beta)}{m_\alpha^2 m_\beta} \ln(\Lambda), \quad \omega_{c\alpha} = \frac{Q_\alpha B}{m_\alpha}, \quad (1.2)$$

which represent the frequency of the plasma oscillations, shortly the plasma frequency, the collision frequency and the cyclotron frequency of the Larmor movement. In the second formula, $\ln(\Lambda)$ denotes the Coulomb logarithm which accounts for small angle collisions. The collective behaviour de facto means fulfilling the condition $\nu \ll \omega_{pe}$.

From the latter formulas it is obvious that a plasma is characterised mainly by the density n , the temperature T and also in a tokamak device by the magnetic field B . The temperature of a plasma can be derived from the Maxwell velocity distribution function. The relation between the mean kinetic energy and the temperature takes the form $E_m = \frac{1}{2} k_B T$ for each degree of freedom. For that reason the temperature can be estimated as the energy corresponding to $k_B T$ and the conversion

$$1 \text{ eV} = 11600 \text{ K} \quad (1.3)$$

can be used.

In the space, plasma occurs in various forms in the density range $10^4 - 10^{35} \text{ m}^{-3}$ and the temperature range $10^{-4} - 10^9 \text{ eV}$. In tokamak devices we observe plasmas typically with densities $10^{18} - 10^{21} \text{ m}^{-3}$ and temperatures $1 - 10^4 \text{ eV}$.

1.2 Tokamak

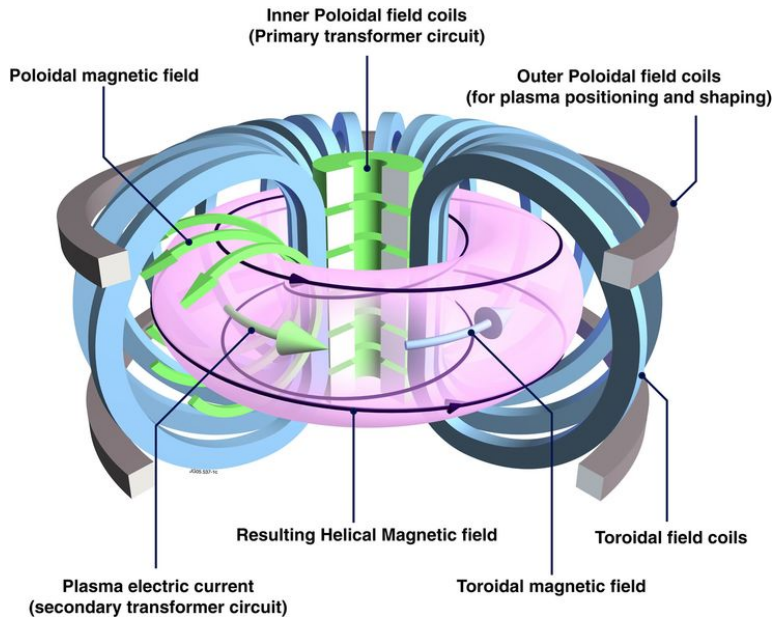


Figure 1.1: Tokamak scheme. [2]

Tokamak (abbreviation of the russian "toroidalnaja kamera i magnitnitnie katushki") is a toroidal device for the plasma confinement using magnetic fields. The magnetic field prevents the contact between the plasma inside and the tokamak vessel. The toroidal magnetic field \mathbf{B}_ϕ is produced by the currents in the toroidal field coils. Because of the toroidal field incapability to confine the plasma, a poloidal magnetic field \mathbf{B}_p is needed as well. It is created by the toroidal plasma current and outer poloidal field coils. The combination of the fields results in the helical magnetic field which holds the plasma inside the chamber. This can be seen in Figure 1.1. [3][4]

Because of this description it is obvious that the main parts of the tokamak are the toroidal and poloidal field coils and the central solenoid (electromagnet) together with the vacuum vessel (chamber). The toroidal field coils geometry causes a stronger toroidal field B_ϕ on the inner side closer to the centre of the tokamak called the high field side (HFS). The region further away from the centre of the tokamak is called the low field side (LFS). Within the tokamak vessel, the toroidal field varies as

$$B_\phi \propto \frac{1}{R}. \quad (1.4)$$

Mainly due to this feature, the cross-section of the tokamak has been modified from the circle to the D-shape. It secures a larger volume of plasma to sit in stronger magnetic field area which seems to make a better performance.

As it was mentioned earlier, the poloidal field \mathbf{B}_p is generated by the toroidal plasma current (the Ampere's law). This field is typically an order of magnitude smaller than the toroidal field. It results in a low helicity, a charged particle performs one cycle in the poloidal direction and multiple ones in the toroidal direction. The number of cycles in the toroidal direction divided by the poloidal ones is denoted as the safety factor q . If q is an irrational number, the trajectory of the particle never crosses itself and creates a coherent surface. Magnetic field lines lie on the surface of a constant characteristic poloidal magnetic flux ψ given as

$$\psi = \int \mathbf{B}_p \cdot d\mathbf{S}. \quad (1.5)$$

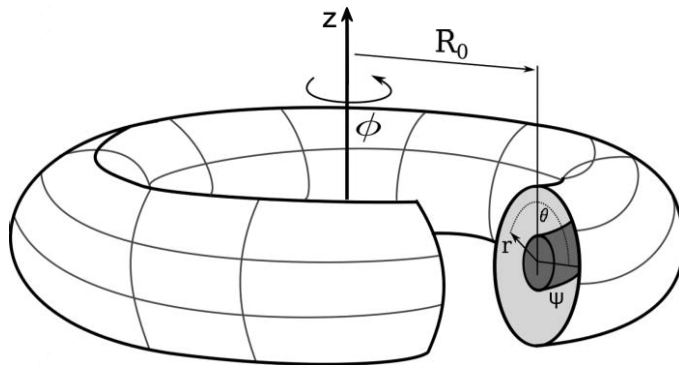


Figure 1.2: Scheme of the tokamak topology. Reproduced from [5] and edited.

Various coordinate systems are used in tokamak research. The most common are the standard cylindrical coordinates (R, ϕ, z) where R is the radius from the main axis, z is the vertical distance from the plane of top-bottom symmetry and ϕ is the toroidal angle. The condition $\phi = \text{const}$ defines the poloidal cross-section. Majority of quantities are symmetric with respect to this angle due to the toroidal symmetric system. Only the toroidal field coils are discrete along the toroidal angle. Because of that, the coordinate origin can be set in the magnetic axis location where $B_p = 0$ at $[R_0, z_0]$ and the polar-like coordinates (r, θ) can be used where r is the minor radius and θ is the poloidal angle. It is favourable for the tokamaks with the circular cross-section, for the tokamaks with a different cross-section than the circular one, it is more convenient to use the normalized poloidal magnetic flux coordinate $\bar{\psi}$ than the minor radius r .

Magnetic flux surfaces are not always closed inside the tokamak vessel. If the particle diffuses to the trajectory on this flux surface, it will inevitably crash into the tokamak first wall. The last closed flux surface (LCFS) is defined as the very edge of the confined plasma. The coordinate corresponds to $\bar{\psi} = 1$ at this surface. The region where flux surfaces are no longer closed inside the tokamak is called a scrape-of-layer (SOL).

Chapter 2

Runaway Electrons

The toroidal electric field is the source of most of the plasma current and the E field existence is also an essential condition for a runaway electron (RE) generation. These electrons represents a serious threat to the first wall of tokamak devices.

The majority of the collisions between charged particles is managed by the long-range, small-angle Coulomb scattering. The electron collision frequency for this small-angle scattering is given by the following formula from (1.2)

$$\nu_{ee} = \frac{n_e e^4}{4\pi \epsilon_0^2 m_e^2 v^3} \ln(\Lambda), \quad (2.1)$$

The expression $\ln(\Lambda)$ stands for the Coulomb logarithm defined as

$$\ln(\Lambda) = \ln\left(\frac{\lambda_D}{b_0}\right), \quad (2.2)$$

where b_0 is the critical collision parameter, i.e. parameter in which the scattering angle equals exactly 90° .

As it can be seen, the collision frequency rapidly decreases with the increasing particle velocity. This is the reason why the frictional force caused by the collisions is not capable to compensate the influence of the induced electric force in the high-energy electron case. Such electrons are incessantly accelerated and "run away" in the velocity phase space.

Studying runaways has numerous reasons throughout the theoretical and experimental plasma physics. Nowadays, theories that result in non-linear effects can describe REs quite successfully. On the other hand, the questions about the collective and global behaviour remains unanswered. This physical effect often influences most of the complex plasma physics of tokamaks, for example the plasma transport, field perturbations impact, confinement quality and MHD instabilities. As it was mentioned earlier, the runaways could represent a serious danger for the first wall of ITER and other larger tokamak facilities. It is a threat for the diagnostics inside the vacuum vessel as well. [6][7]

2.1 Runaway Electron Generation

Runaway electron generation may have multiple causes. In the first stage of this generation we talk about runaway seed, a little number of high-energy electrons. The seed may be produced by cosmic particles, tritium decay, instabilities, Compton scattering of photons on wall atoms or resonance with plasma waves. Nevertheless, the principal processes of this so called primary generation mechanisms are the Dreicer mechanism and the hot-tail mechanism. The secondary mechanism is based on multiplying the generated seed by the close collisions and it is called the avalanche mechanism.

2.1.1 Dreicer Mechanism

The primary generation of runaway electrons is caused by the frictional force insufficient capability to compensate the induced electric force. The condition for the electron runaway in a plasma was first introduced and described by H. Dreicer with his Dreicer field, which is given as

$$E_D = \frac{n_e e^3}{4\pi\epsilon_0^2 k_B T_e} \ln(\Lambda). \quad (2.3)$$

The Dreicer field E_D (in original papers [8],[9] denoted as critical field E_c) represents the minimum of the electric field in which the electron velocity exceeds the plasma thermal velocity in the average period between collisions.

From the simplified situation it is possible to derive the critical velocity and critical field formula. An electron in a plasma experiences the force equal to $\mathbf{F}_e = -e\mathbf{E}$ and the drag force resulting from Coulomb interactions, conveniently written in the form

$$\mathbf{F}_d = m_e \mathbf{v} \nu_{\text{coll}}(v), \quad (2.4)$$

where $\nu_{\text{coll}}(v)$ is the collision frequency given in (2.1). The non-relativistic movement of an electron in the direction parallel to the electric field \mathbf{E} can be written as

$$m_e \frac{dv}{dt} = eE - m_e v \nu_{\text{coll}}(v) = eE - \frac{n_e e^4 \ln(\Lambda)}{4\pi\epsilon_0^2 m_e v^2}. \quad (2.5)$$

It is obvious that in the case of $\frac{dv}{dt} > 0$, electrons are accelerated due to the electric field. If there is no other force causing a deceleration (such as radiation losses) Figure 2.1, the generation of the runaway electrons occurs in the critical electric field

$$E_c = \frac{n_e e^3}{4\pi\epsilon_0^2 m_e c^2} \ln(\Lambda). \quad (2.6)$$

At least some electrons are accelerated when the electric field is over the critical field E_c (current designation). The relation for the critical field lacks the dependence on the electron temperature and in most experiments, the value of the experimental critical field is higher [10].

The critical velocity

$$v_c = \sqrt{\frac{n_e e^3 \ln \Lambda}{4\pi \epsilon_0^2 m_e E}} \quad (2.7)$$

represents the threshold where the frictional force equals the electric field force Figure 2.2.

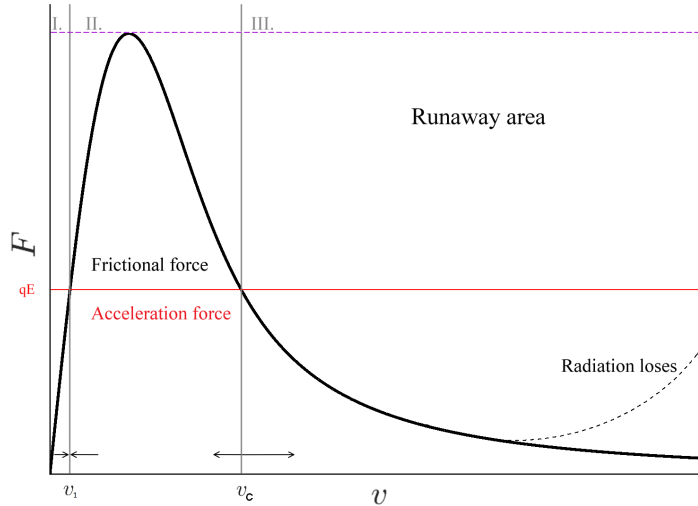


Figure 2.1: Illustration of the electron affecting forces. The dashed line represents the Dreicer field. [11]

The Dreicer mechanism of the RE generation is more likely to appear for smaller tokamak devices with a larger loop voltage and lower density. This is the case of COMPASS. In such tokamaks the electric field overcomes the critical field at least during the breakdown. Part of the runaway population that is created could be directly released but most of it stays confined [11].

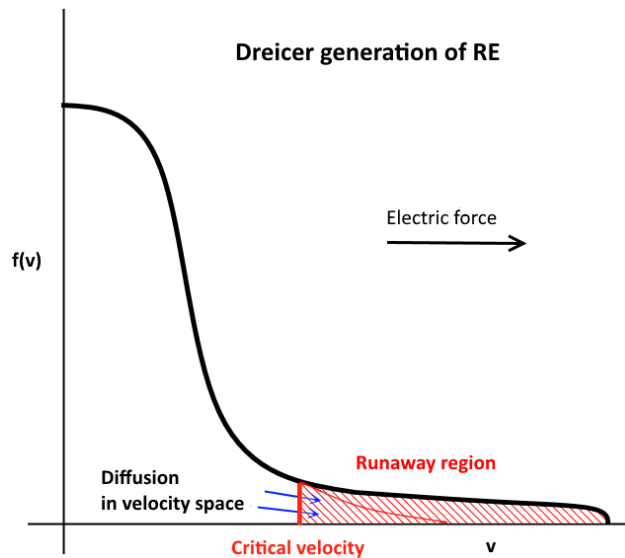


Figure 2.2: Scheme of the RE production caused by the Dreicer mechanism, $f(v)$ represents distribution function. Used with permission of O. Ficker.

2.1.2 Hot-tail Mechanism

The so called hot-tail mechanism is different from the one described above. It occurs mainly in plasma disruptions. These situations, which are characterized by a steep decrease of the plasma current, may have multiple causes.

In the case of the radiative disruption, the most important disruption in the RE studies. Released parts of the first wall may be the source of such disruption. We are also able to induce the runaways in tokamaks by the injection of a high Z gas or pellets. When these impurities penetrate a plasma, there supervenes the thermal quench. Thermal electrons lose their energy owing to the ionisation and excitation of the impurity atoms, the plasma conductivity decreases and the current quench occurs. However, the fast non-thermal electrons are not decelerated due to their small collisional frequency. They appear in the runaway region and are further accelerated by the increased toroidal electric field.

The sudden plasma parameters change also changes the Dreicer field. With a lower electron temperature T_e , the value E_D considerably rises so the electric field affects only the fast collisionless electrons [12]. This effect is shown in Figure 2.3. The hot-tail mechanism is relevant even in the case of some particular instabilities and can generate a large population of the runaways.

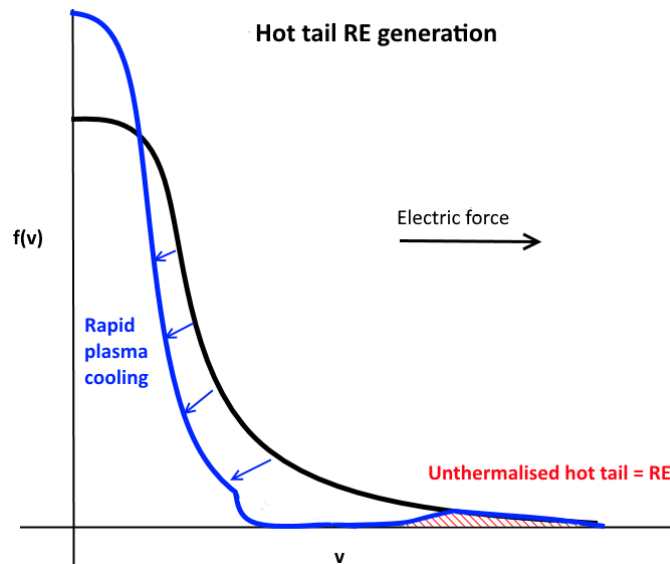


Figure 2.3: Scheme of the RE production caused by the hot-tail mechanism, used with permission of O. Ficker.

2.1.3 Secondary Mechanism

It was determined that the Dreicer mechanism is not able to generate a large runaway population that was observed in experiments with rather low electric fields. Some other secondary mechanism has to be taken into account.

The condition for the secondary RE generation mechanism is an initial RE existence in a plasma. Secondary runaways are produced with an exponential grow rate [10]

$$\gamma_{\text{sec}} \propto \left(\frac{E}{E_c} - 1 \right) \quad (2.8)$$

due to the knock-on collisions. These are thermal electron and fast electron close collisions with a small impact parameter. In this situation, a large amount of the parallel momentum is being transported. The thermal electron gains a velocity higher than the critical velocity v_c (2.7) and it is pushed to the runaway region. This mechanism is also called the "*avalanche mechanism*" because of its development character. One RE can affect several other electrons and they act as the primary ones. The energy of the created electron is around 10-20 MeV. [13]

In present-day, tokamaks with plasma currents around 1 MA, the avalanche mechanism does not represent such a threat unlike in the planned large tokamak ITER. Theories and simulations predict massive runaway formations in ITER-like conditions (amplification factor e^{50}). It makes the avalanche mechanism the most dangerous issue in the ITER tokamak.

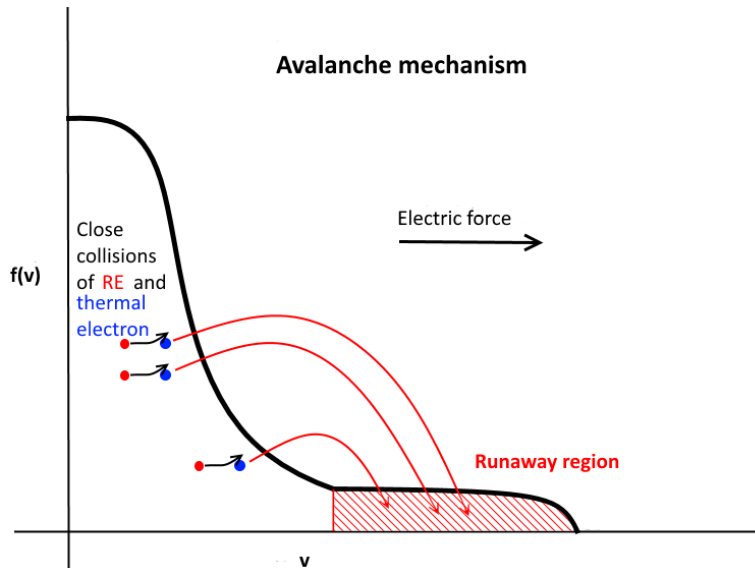


Figure 2.4: Scheme of the RE production caused by the avalanche mechanism, used with permission of O. Ficker.

2.2 Runaway Electron Diagnostics

In this section, the main runaway electron detection approaches will be introduced. Runaway electrons diagnostic methods can be divided into two groups. The first one measures the consequences of the high-energetic electron impact into the tokamak first wall or a detector outside of the tokamak vessel. Such methods measure runaway losses. The second group focuses on radiative effects of the charged particle movement and they are able to measure properties of the REs confined inside a tokamak.

Radiative Effects

Bremsstrahlung. If the electron movement is not linear and uniform the electromagnetic radiation occurs. The continuum radiation historically called the "*bremsstrahlung*" arises from electron-ion collisions. The kinetic energy electron loss during the collision is compensated by this radiation. For the runaway electron with a relativistic velocity, the energy loss by the bremsstrahlung is more substantive than the momentum loss during the collision. This radiation is detected in the soft X-ray (SXR) range of frequencies.

Synchrotron Radiation. When a charged particle is placed into a magnetic field, its movement is not linear and the particle emits the synchrotron radiation. It has the same source as the above mentioned bremsstrahlung and it occurs due to the toroidal movement in a tokamak. The frequencies of the synchrotron radiation are in the infra red (IR) spectrum range, in larger devices even in the visible spectrum. Using a tangentially placed fast IR camera with the line-view opposite to the plasma current may be useful for the RE synchrotron radiation measurement. With a good spatial and temporal resolution it is possible to measure the position of the beam and its change during a discharge. The RE distribution function could be possibly determined with this diagnostic method.

Electron Cyclotron Emission. This method uses the same radiative principle as the synchrotron radiation with one difference. The electron cyclotron emission appears due to the Larmor rotation around the magnetic field line. This diagnostic method will be further described in subsection 3.5.1.

Runaway Losses

Cherenkov Radiation. The electromagnetic so called *Cherenkov radiation* is emitted in the case of a charged particle (such as an electron) passing through a dielectric medium at the speed greater than the phase velocity of the light in that medium v_f . It is released into the shock cone, similarly to the supersonic shock wave, with the axisymmetry along the direction of the particle movement with the cone angle θ given as

$$\cos \theta = \frac{1}{N\beta} \quad \text{with} \quad \beta = \frac{v_f}{c}, \quad (2.9)$$

where c is the speed of light in vacuum and N is the refractive index in the medium. The frequencies of the Cherenkov radiation are in the visible spectrum with peaks in the UV region. Cherenkov detectors contain a dense material (usually diamond, TiO₂, etc.) through which a relativistic electron can pass. The emitted radiation is then converted to the electric output and amplified by a photomultiplier. The detector has to be placed inside the tokamak vessel to be sure that the electron hits the detector before any other material. It is difficult to secure the limitation of the hard X-ray photon influence. The advantages of this diagnostic method are the great temporal resolution and the ability to estimate the parallel velocity distribution function.

Interaction with the Tokamak Wall. Runaways are not always well confined and some of them could be released. Fast electrons then hit the limiter or the first wall. One of the possible consequences is emitting a high-energetic electromagnetic radiation with frequencies in the hard X-ray (HXR) region. In the contact with the dense matter of the first wall or limiter, electrons undergo an inelastic scattering on the nucleus and are strongly decelerated. They emit energy in the form of the bremsstrahlung radiation proportional to the atomic number squared Z_i^2 . This process dominates for electron energies larger than 11 MeV. For electron energies under 11 MeV also takes place inelastic scattering on bounded electrons. The hard X-ray diagnostics prove the existence of REs in the plasma. With a proper calibration it is possible to estimate the distribution function, but it has to be kept in mind that there are different HXR sources as well.

The HXR photons can leave the tokamak and be measured or undergo a series of absorptions and re-radiations. According to the photon energy they can even trigger some nuclear reactions. In the energies about 10 MeV the collision between photon and nucleus sometimes leads to the neutron production. During the collision the nucleus experiences a giant dipole resonance ending with the fission or releasing a neutron. These neutrons are called photoneutrons and they can be detected as well. Taking into account the first wall material the most common reactions are $^{12}\text{C}(\gamma, n)^{11}\text{C}$ and $^9\text{Be}(\gamma, n)^8\text{Be}$.

All discussed phenomenons are shown in Figure 2.5.

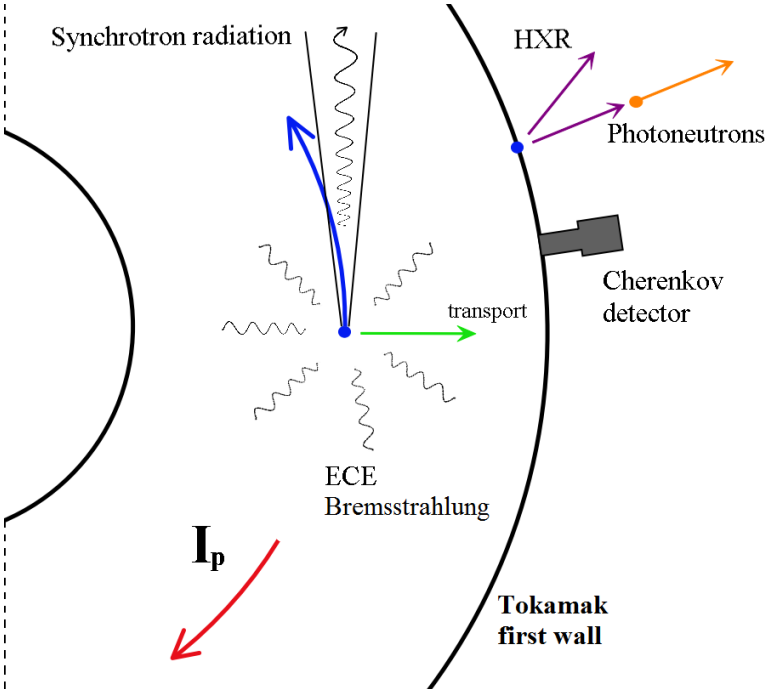


Figure 2.5: Scheme of all kinds of the RE radiation. Top view of the tokamak.

Chapter 3

Waves in Plasma

In the following pages the theory of waves in plasma will be described from the basic plasma oscillations to the electromagnetic waves in cold magnetized plasma and brief theory of the waves in hot plasma.

Electromagnetic waves are a useful tool for plasma diagnostics, for example the interferometry, reflectometry and radiometry, and for additional ion or electron cyclotron resonant heating systems (ICRH, ECRH) and current drive (ECCD). All these systems seem to be necessary for a regular operation of ITER and the future demonstration fusion power station, DEMO. The wave-plasma interaction knowledge is crucial for the proper device design and data analysis.

In the following derivations we will use the perturbation calculus. All quantities can be divided into the zero-order quantity part, which is static and uniform, and the first-order quantity part. This is so called perturbation, which is assumed to vary as $\exp[i(\mathbf{k} \cdot \mathbf{r} - \omega t)]$, where \mathbf{k} is the wave vector, ω the frequency and \mathbf{r} , t is the position and time. The high order terms are neglected if we consider a low perturbation amplitude [14]. Thus the quantities can be written as

$$\begin{aligned} n_e &= n_{e0} + \delta n_e = n_{e0} + n_{e1}e^{i(\mathbf{k} \cdot \mathbf{r} - \omega t)}, \\ \mathbf{v}_e &= \mathbf{v}_{e0} + \delta \mathbf{v}_e = \mathbf{v}_{e0} + \mathbf{v}_{e1}e^{i(\mathbf{k} \cdot \mathbf{r} - \omega t)}, \\ \mathbf{E} &= \mathbf{E}_0 + \delta \mathbf{E} = \mathbf{E}_0 + \mathbf{E}_1e^{i(\mathbf{k} \cdot \mathbf{r} - \omega t)}. \end{aligned} \quad (3.1)$$

The Fourier transform is always performed after the perturbation calculus. It transforms differential operators of a first-order scalar quantity f and a vector quantity \mathbf{V} as following [15]

$$\begin{aligned} \frac{\partial f}{\partial t} &= -i\omega f, & \nabla^2 f &= -k^2 f, \\ \nabla f &= i\mathbf{k}f, & \nabla \cdot \mathbf{V} &= i\mathbf{k} \cdot \mathbf{V}, & \nabla \times \mathbf{V} &= i\mathbf{k} \times \mathbf{V}. \end{aligned} \quad (3.2)$$

3.1 Plasma Oscillations

Plasma oscillations are a fundamental type of a wave in a plasma. In the situation where a cloud of electrons is shifted towards the homogeneous ion background, an electric field is created. This field pushes the electrons back to the equilibrium position. The electrons start to make oscillations due to their inertia.

The frequency of these oscillations is given as the electron plasma frequency in (1.2) and can be derived from the linearised motion equation

$$m_e \frac{\partial \mathbf{v}_e}{\partial t} = -e\mathbf{E}, \quad (3.3)$$

the continuity relation

$$\frac{\partial n_e}{\partial t} + \nabla \cdot (n_e \mathbf{v}_e) = 0, \quad (3.4)$$

and the Maxwell equations in the SI units

$$\begin{aligned} \nabla \cdot \mathbf{E} &= \frac{\rho}{\varepsilon_0}, & \nabla \times \mathbf{B} - \mu_0 \varepsilon_0 \frac{\partial \mathbf{E}}{\partial t} &= \mu_0 \mathbf{j}, \\ \nabla \cdot \mathbf{B} &= 0, & \nabla \times \mathbf{E} + \frac{\partial \mathbf{B}}{\partial t} &= 0. \end{aligned} \quad (3.5)$$

The frequency is high enough to consider the ions motionless because the heavy ions can't react to the fast changing electric field. Thus, the dispersion relation of the plasma oscillations can be obtained from (3.3), (3.4) and the first equation (electrostatic) in (3.5) using the perturbation calculus and Fourier transform resulting in the system

$$\begin{aligned} -im\omega v_{e1} &= -eE_1, \\ -i\omega n_{e1} &= n_{e0} ikv_{e1}, \\ ik\varepsilon_0 E_1 &= -en_{e1}. \end{aligned} \quad (3.6)$$

The resulting dispersion relation is in the form

$$\omega = \omega_{pe} = \sqrt{\frac{n_e e^2}{m_e \varepsilon_0}} \quad (3.7)$$

A thermal movement of the electrons passes information from the oscillation further in the plasma and creates the plasma wave [1]. We can obtain the dispersion relation from the same equations when the pressure element is added to the motion equation which is in the modified form

$$m_e n_e \frac{\partial \mathbf{v}_e}{\partial t} = -en_e \mathbf{E} - \nabla p_e = -en_e \mathbf{E} - 3k_B T_e \nabla n_e. \quad (3.8)$$

It yields

$$\omega^2 = \omega_{pe}^2 + \frac{3}{2} k^2 v_{Te}^2, \quad (3.9)$$

where v_{Te} is the thermal electron velocity value in the form $v_{Te} = \sqrt{\frac{2k_B T_e}{m_e}}$ and k is the wave vector magnitude.

3.2 Waves in Unmagnetized Plasma

The source of waves in plasma could be an incident electromagnetic wave. The simplest case is a plasma without an external magnetic field. In vacuum the dispersion relation is in the form $\omega^2 = c^2 k^2$ for electromagnetic waves, where c is the speed of light. The difference between vacuum and a plasma is the occurrence of the perturbation currents caused by the charged particle movement. If the electromagnetic wave frequency is high enough, the currents are only the consequences of an electron movement as following

$$\mathbf{j} = -n_e e \mathbf{v}_e. \quad (3.10)$$

By the similar procedure as indicated above we can get the dispersion relation slightly modified from the vacuum case as

$$\omega^2 = \omega_{pe}^2 + c^2 k^2. \quad (3.11)$$

The most important is the existence of the so called cutoff frequency. If we emit the wave with $\omega < \omega_{pe}$ into the plasma with the plasma frequency ω_{pe} , the wave vector value k is an imaginary number. The wave is not capable of a propagation in the plasma, it is exponentially damped and reflected back.

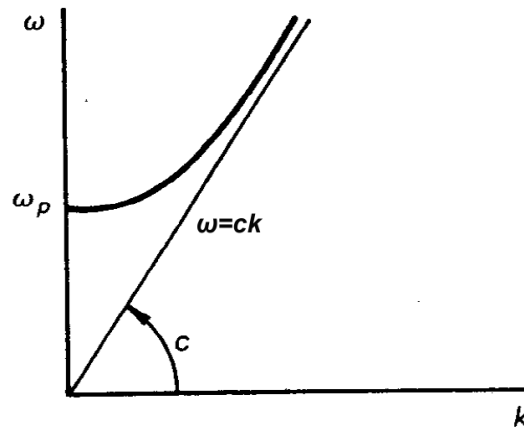


Figure 3.1: Dispersion relation for electromagnetic waves in unmagnetized plasma. Reproduced from [1] and edited.

3.3 Waves in Cold Magnetized Plasma

3.3.1 Dielectric Tensor

This section is focused on the high-frequency wave propagation in a plasma in a homogeneous magnetic field. Collisions are neglected for the sake of simplicity. In reality, collisions in a hot plasma lead to a weak damping. Only high frequency waves are considered so the ions are static.

It is favourable to include the current density \mathbf{j} into the electric displacement vector \mathbf{D} , which means the current density in a dielectric is taken as a charge displacement consequence. The Ampere law becomes

$$\nabla \times \mathbf{B} = \frac{1}{c^2} \frac{\partial \mathbf{D}}{\partial t}. \quad (3.12)$$

We can get the electric displacement formula from the premise (3.1) for the current density and from the Faraday law in the form

$$\mathbf{D} = \mathbf{E} + \frac{i}{\varepsilon_0 \omega} \mathbf{j} = \boldsymbol{\varepsilon} \cdot \mathbf{E}. \quad (3.13)$$

The important relation results from the previous formula and the current density definition

$$\mathbf{j} = -n_e e \mathbf{v} = \boldsymbol{\sigma} \cdot \mathbf{E} = i \varepsilon_0 \omega (\mathbf{I} - \boldsymbol{\varepsilon}) \cdot \mathbf{E}, \quad (3.14)$$

where $\boldsymbol{\varepsilon}$ denotes the dielectric tensor and $\boldsymbol{\sigma}$ electric conductivity.

The components of this dielectric tensor are not all independent. This attribute can be validated by using the Cartesian coordinate system (x, y, z) in which an external magnetic field is along the coordinate z and the wave vector \mathbf{k} is in the (x, z) plane which means $\mathbf{k} = k_{\perp} \hat{\mathbf{x}} + k_{\parallel} \hat{\mathbf{z}}$. Reversing the \mathbf{B}_0 and \mathbf{k} direction is equivalent to the rotation of the reference frame by 180° about the y axis. Thus, the dielectric tensor has only six independent components, as it is shown in [14]. If there is independence of the $\boldsymbol{\varepsilon}$ on the \mathbf{k} , therefore the rotation invariance about the z axis, the dielectric tensor can be written in the form

$$\boldsymbol{\varepsilon}(\omega, \mathbf{B}_0) = \begin{pmatrix} \varepsilon_{11} & \varepsilon_{12} & 0 \\ -\varepsilon_{12} & \varepsilon_{11} & 0 \\ 0 & 0 & \varepsilon_{33} \end{pmatrix}. \quad (3.15)$$

Now, we need to solve the motion equation in the electromagnetic field for finding the components of the dielectric tensor. The motion equation in the electromagnetic field is

$$-i\omega m_e \mathbf{v}_e = -e(\mathbf{E} + \mathbf{v}_e \times \mathbf{B}_0), \quad (3.16)$$

where \mathbf{B}_0 is the constant external magnetic field, thus the zero-order quantity on the other hand \mathbf{E} and \mathbf{v}_e are the first-order quantities. Because of this,

the indexing can be omitted. If the coordinate system is chosen so that the magnetic field is along the z axis ($\mathbf{B}_0 = \hat{\mathbf{z}}B_0$), three components of (3.16) are

$$\begin{aligned} v_x &= -i \frac{1}{B_0} \frac{\omega_{ce}}{\omega} \frac{1}{1 - \frac{\omega_{ce}^2}{\omega^2}} \left(E_x - i \frac{\omega_{ce}}{\omega} E_y \right), \\ v_y &= -i \frac{1}{B_0} \frac{\omega_{ce}}{\omega} \frac{1}{1 - \frac{\omega_{ce}^2}{\omega^2}} \left(E_y + i \frac{\omega_{ce}}{\omega} E_x \right), \\ v_z &= -i \frac{1}{B_0} \frac{\omega_{ce}}{\omega} E_z, \end{aligned} \quad (3.17)$$

where

$$\omega_{ce} = \frac{eB_0}{m_e} \quad (3.18)$$

is the electron cyclotron frequency. Together with (3.14) we can get the components of the dielectric vector

$$\varepsilon_{11} = 1 - \frac{X}{1 - Y^2}, \quad \varepsilon_{12} = i \frac{XY}{1 - Y^2}, \quad \varepsilon_{33} = 1 - X \quad (3.19)$$

with $X = (\omega_{pe}/\omega)^2$ and $Y = \omega_{ce}/\omega$ [14].

3.3.2 Dispersion Relation

The dispersion relation derivation in a cold plasma remains unsolved. From the Faraday and modified Ampere law (3.12) the wave equation for wave electric field comes out as

$$\nabla \times (\nabla \times \mathbf{E}) + \frac{1}{c^2} \frac{\partial^2}{\partial t^2} (\boldsymbol{\varepsilon} \cdot \mathbf{E}) = 0, \quad (3.20)$$

which is altered for the perturbed quantities into the system of the homogeneous linear equations

$$\mathbf{k} \times (\mathbf{k} \times \mathbf{E}) + \frac{\omega^2}{c^2} \boldsymbol{\varepsilon} \cdot \mathbf{E} = 0. \quad (3.21)$$

Without a loss of a generality we can take the latter used coordinate system, the system $\mathbb{D} \cdot \mathbf{E} = 0$ then simplifies to the system where

$$\mathbb{D} = \begin{pmatrix} -k_{\parallel}^2 & 0 & k_{\perp} k_{\parallel} \\ 0 & -k_{\perp}^2 - k_{\parallel}^2 & 0 \\ k_{\parallel} k_{\perp} & 0 & -k_{\perp}^2 \end{pmatrix} + \frac{\omega^2}{c^2} \begin{pmatrix} \varepsilon_{11} & \varepsilon_{12} & 0 \\ -\varepsilon_{12} & \varepsilon_{11} & 0 \\ 0 & 0 & \varepsilon_{33} \end{pmatrix}. \quad (3.22)$$

The condition of a non-trivial solution existence for this system, $\det(\mathbb{D}) = 0$, provides the solution in form

$$\begin{aligned} \det(\mathbb{D}) = D(\mathbf{k}, \omega) &\equiv \frac{c^4}{\omega^4} k_{\perp}^4 \varepsilon_{11} - \frac{c^2}{\omega^2} k_{\perp}^2 \left[\varepsilon_{12}^2 + (\varepsilon_{11} + \varepsilon_{33}) \left(\varepsilon_{11} - \frac{c^2}{\omega^2} k_{\parallel}^2 \right) \right] \\ &+ \varepsilon_{33} \left[\left(\varepsilon_{11} - \frac{c^2}{\omega^2} k_{\parallel}^2 \right)^2 + \varepsilon_{12}^2 \right] = 0. \end{aligned} \quad (3.23)$$

This equation is bi-quadratic. If we introduce φ as the angle between \mathbf{B}_0 and \mathbf{k} , it is possible to write $k_{\perp} = k \sin \varphi$ and $k_{\parallel} = k \cos \varphi$. Together with the introduction of the optical index

$$\mathbf{N} = \frac{\mathbf{k}c}{\omega} \quad (3.24)$$

the solution of (3.23) can be written in the form of the Appelton-Hartree formula

$$N^2 = 1 - \frac{2X(1-X)}{2(1-X) - Y^2 \sin^2 \varphi \pm [Y^4 \sin^4 \varphi + 4Y^2(1-X)^2 \cos^2 \varphi]^{1/2}}. \quad (3.25)$$

These formulas are provided in many articles in the Stix's notation [16][17][18], where the dielectric tensor is in the form

$$\varepsilon(\omega, \mathbf{B}_0) = \begin{pmatrix} S & iD & 0 \\ -iD & S & 0 \\ 0 & 0 & P \end{pmatrix}, \quad (3.26)$$

where

$$S = \frac{1}{2}(R+L), \quad D = \frac{1}{2}(R-L), \quad (3.27)$$

$$R = 1 - \frac{\omega_{pe}^2}{\omega(\omega - \omega_{ce})}, \quad (3.28)$$

$$L = 1 - \frac{\omega_{pe}^2}{\omega(\omega + \omega_{ce})}, \quad (3.29)$$

$$P = 1 - \frac{\omega_{pe}^2}{\omega^2}. \quad (3.30)$$

The dispersion relation is the solution of the system

$$\begin{aligned} AN^4 + BN^2 + C &= 0, \\ A &= S \sin^2 \varphi + P \cos^2 \varphi, \\ B &= RL \sin^2 \varphi + PS(1 + \cos^2 \varphi), \\ C &= PRL, \end{aligned} \quad (3.31)$$

and the Appelton-Hartree formula becomes

$$N^2 = \frac{B \pm F}{2A} \quad (3.32)$$

where

$$F^2 = (RL - PS)^2 \sin^4 \varphi + 4P^2 D^2 \cos^2 \varphi. \quad (3.33)$$

3.3.3 Polarizations

Let us analyse the dispersion relation. In the elementary case of the wave propagation parallel to \mathbf{B}_0 ($\varphi = 0$) we can find, besides the plasma oscillations (3.7), two circular wave modes.

$$N_{R,L}^2 = 1 - \frac{X}{1 \mp Y},$$

$$\begin{aligned} \text{in the Stix's notation} \quad N_R^2 = R, \quad N_L^2 = L, \\ \text{with polarizations} \quad \frac{E_x}{E_y} = \mp i, \quad E_z = 0. \end{aligned} \tag{3.34}$$

For the relation with the $-$ sign we get the right-hand mode (R-mode) where the electric field $\delta\mathbf{E}$ rotates clockwise, in the other case we talk about the left-hand mode (L-mode) where the electric field rotates anticlockwise. In both cases an observer is looking along the direction of the wave propagation.

In the case of the propagation perpendicular to \mathbf{B}_0 ($\varphi = \pi/2$) we can find again two modes as following

$$N_O^2 = 1 - X,$$

$$\begin{aligned} \text{in the Stix's notation} \quad N_O^2 = P, \\ \text{with polarization} \quad E_x = E_y = 0 \end{aligned} \tag{3.35}$$

and

$$N_X^2 = 1 - \frac{X(1-X)}{1-X-Y^2},$$

$$\begin{aligned} \text{in the Stix's notation} \quad N_X^2 = \frac{RL}{S}, \\ \text{with polarization} \quad \frac{E_x}{E_y} = -i \frac{1-X-Y^2}{XY}, \quad E_z = 0. \end{aligned} \tag{3.36}$$

The first of these modes is called the *ordinary* mode (O-mode) what is the wave with the electric field $\delta\mathbf{E}$ parallel to the external magnetic field \mathbf{B}_0 direction ($\delta\mathbf{E} \parallel \mathbf{B}_0$). It is a transverse linearly polarized wave. Contrarywise, the other is called the *extraordinary* mode (X-mode), which is the wave with the field $\delta\mathbf{E}$ perpendicular to the external magnetic field \mathbf{B}_0 direction ($\delta\mathbf{E} \perp \mathbf{B}_0$). It is an elliptically polarized wave with a non-zero longitudinal component E_x .

In the transition between $\varphi = 0$ and $\varphi = \pi/2$, the nature of the waves changes substantially. [14][18][19]

3.3.4 Cutoffs and Resonances

At this point it is convenient to remind the term **cutoff**. This is the situation when $N^2 = 0$, the wave is not capable of propagation in a plasma. The wave is exponentially damped in the plasma volume, where N is a purely complex number ($N^2 < 0$) and reflected back. From the equations (3.34), (3.35), (3.36) we can obtain the the cutoff conditions as $R = 0$, $L = 0$, $P = 0$ written as following:

$$\begin{aligned}
 \text{Plasma cutoff} \quad \omega &= \omega_O = \omega_{pe}, \\
 \text{Right - hand cutoff} \quad \omega &= \omega_R = \left(\frac{\omega_{ce}^2}{4} + \omega_{pe}^2 \right)^{1/2} + \frac{\omega_{ce}}{2}, \\
 \text{Left - hand cutoff} \quad \omega &= \omega_L = \left(\frac{\omega_{ce}^2}{4} + \omega_{pe}^2 \right)^{1/2} - \frac{\omega_{ce}}{2}.
 \end{aligned} \tag{3.37}$$

In the case of the **resonance**, the optical index $N^2 = \pm\infty$. The wave is at this point fully absorbed. The resonance for $\varphi = 0$ fulfil the condition $R = \pm\infty$ and it is called the electron cyclotron resonance. If we did not neglected the movement of ions at the beginning of this chapter, the ion cyclotron resonance would occurs in the condition $L = \pm\infty$. For $\varphi = \pi/2$ we get $S = 0$, which is the condition for upper hybrid resonance. The fundamental electron cyclotron resonances can be expressed as

$$\begin{aligned}
 \text{Electron cyclotron resonance} \quad \omega &= \omega_{ce}, \\
 \text{Upper hybrid resonance} \quad \omega &= \omega_{UH} = (\omega_{ce} + \omega_{pe})^{1/2}.
 \end{aligned} \tag{3.38}$$

In the model of a cold plasma there is no cyclotron resonance for the perpendicular wave propagation. This phenomenon occurs only in the hot plasma solution.

3.4 Waves in Hot Plasma

In preparation for the subject of the next sections, the relativistic theory of wave propagation in a uniform collisionless plasma in a homogeneous magnetic field will be reviewed. As in the previous theory, we consider only the waves with frequencies in the electron cyclotron range. Ions can be thus treated as a static background.

From the kinetic theory, the relativistic collisionless equation is the one derived by Vlasov in the form

$$\frac{\partial f}{\partial t} + \mathbf{v} \cdot \frac{\partial f}{\partial \mathbf{r}} - e (\mathbf{E} + \mathbf{v} \times \mathbf{B}) \cdot \frac{\partial f}{\partial \mathbf{p}} = 0 \tag{3.39}$$

for the electron distribution function $f(\mathbf{r}, \mathbf{p}, t)$, where \mathbf{v} and \mathbf{p} are the electron velocity and momentum related by

$$\mathbf{p} = \gamma m_e \mathbf{v}. \tag{3.40}$$

The symbol γ denotes the Lorenz factor, thus

$$\gamma = \sqrt{1 + \left(\frac{p}{m_e c}\right)^2} = \left[1 - \left(\frac{v}{c}\right)^2\right]^{-1/2}.$$

To derive the dielectric tensor it is necessary to find the current density induced by the wave

$$\mathbf{J}(\mathbf{r}, t) = -e \int \mathbf{v} f(\mathbf{r}, \mathbf{p}, t) d\mathbf{p}. \quad (3.41)$$

We seek solutions in the form

$$\begin{aligned} f(\mathbf{r}, \mathbf{p}, t) &= f_0(\mathbf{p}) + \delta f(\mathbf{r}, \mathbf{p}, t) \\ \mathbf{E}(\mathbf{r}, t) &= \delta \mathbf{E}(\mathbf{r}, t) \\ \mathbf{B}(\mathbf{r}, t) &= \mathbf{B}_0 + \delta \mathbf{B}(\mathbf{r}, t) \end{aligned} \quad (3.42)$$

We can obtain the Fourier amplitude of the current density by the derivation which is over the scope of this thesis and which can be found in [14][16]

$$\mathbf{j}(\mathbf{k}, \omega) = -i \frac{n_0 e^2}{m_e} \sum_{n=-\infty}^{\infty} \int \frac{\mathbf{S}^{(n)} \cdot \mathbf{E}(\mathbf{k}, \omega)}{\gamma(\omega - n\omega_{ce} - k_{\parallel} v_{\parallel})} d\mathbf{p} \quad (3.43)$$

where n_0 is the equilibrium density and $\mathbf{S}^{(n)}$ is tensor

$$\mathbf{S}^{(n)} = \begin{pmatrix} p_{\perp} \left(\frac{nJ_n}{\rho}\right)^2 F_{\perp} & -ip_{\perp} \left(\frac{nJ_n J'_n}{\rho}\right) F_{\perp} & p_{\parallel} \left(\frac{nJ_n^2}{\rho}\right) F_{\perp} \\ ip_{\perp} \left(\frac{nJ_n J'_n}{\rho}\right) F_{\perp} & p_{\perp} (J'_n)^2 F_{\perp} & ip_{\parallel} (J_n J'_n) F_{\perp} \\ p_{\parallel} \left(\frac{nJ_n^2}{\rho}\right) F_{\perp} & -ip_{\parallel} (J_n J'_n) F_{\perp} & p_{\parallel} (J_n)^2 F_{\parallel} \end{pmatrix}, \quad (3.44)$$

where $J_n = J_n(\rho)$ is the Bessel function of the first kind, $\rho = k_{\perp} v_{\perp} / \omega_{ce}$ and

$$\begin{aligned} F_{\perp} &= \frac{\partial f_0}{\partial p_{\perp}} + \frac{k_{\parallel} v_{\perp}}{\omega} \left(\frac{\partial f_0}{\partial p_{\parallel}} - \frac{p_{\parallel}}{p_{\perp}} \frac{\partial f_0}{\partial p_{\perp}} \right), \\ F_{\parallel} &= \frac{\partial f_0}{\partial p_{\parallel}} - n \frac{\omega_{ce}}{\omega} \left(\frac{\partial f_0}{\partial p_{\parallel}} - \frac{p_{\parallel}}{p_{\perp}} \frac{\partial f_0}{\partial p_{\perp}} \right). \end{aligned} \quad (3.45)$$

It is important to notice that the largest contribution into the integral in (3.44) comes from the waves fulfilling the resonant condition

$$\omega - n\omega_{ce} - k_{\parallel} v_{\parallel} \approx 0. \quad (3.46)$$

Finally, from (3.14) we get the dielectric tensor

$$\varepsilon(\mathbf{k}, \omega) = \mathbf{I} + \frac{\omega_{pe}^2}{\omega} \sum_{n=-\infty}^{\infty} \int \frac{\mathbf{S}^{(n)}}{\gamma(\omega - n\omega_{ce} - k_{\parallel} v_{\parallel})} d\mathbf{p} \quad (3.47)$$

In the solution of such dielectric tensor occurs a singularity which can be calculated by using the Cauchy principal value. This singularity appears in the velocity phase space where the resonant condition (3.46) is exactly fulfilled. It is the reason of the cyclotron waves emission independent on the wave vector direction. [14]

3.5 Electron Cyclotron Waves

Every electron moving in an external magnetic field emits electromagnetic radiation (sometimes also called the *magnetic bremsstrahlung*) at the cyclotron frequency, *electron cyclotron emission* (ECE). Circular movement with the Larmor radius along a magnetic induction line causes this behaviour. If the electron dynamics is taken to be non-relativistic, at the first moment it may seem that the emission (or absorption) is possible only when the frequency of the emitted (or absorbed) wave is the same as ω_{ce} in (3.18).

However, the finiteness of the Larmor radius implies that the electromagnetic field generated by an electron gyrating with the cyclotron frequency is not simply harmonic hence higher harmonics $n\omega_c$ emerge. Thanks to the relativistic effects, distribution function and Doppler effect, the emitted frequencies have a fairly wide spectrum Figure 3.2. The frequency at which an electron moving with a velocity \mathbf{v} is able to emit or absorb the waves having a wave vector \mathbf{k} , through the n -th harmonic contribution, is given by (3.46)

$$\omega = n \cdot \omega_{ce}(B, v) + k_{\parallel}v_{\parallel} = n \cdot \omega_{ce}(B)/\gamma + k_{\parallel}v_{\parallel}. \quad (3.48)$$

The relativistic effects are represented by the Lorentz gamma factor. The second term on the right hand side denotes the longitudinal Doppler effect, the index \parallel indicates the component parallel to \mathbf{B}_0 . [20][14]

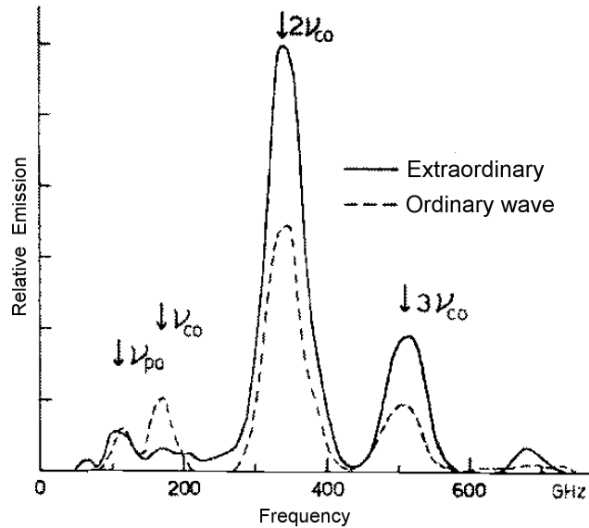


Figure 3.2: Typical cyclotron emission spectra from a tokamak plasma when $\omega_p < \omega_c$. ν_{po} a $n \cdot \nu_{co}$ denotes the plasma and harmonic cyclotron frequency [21].

In a spatially varying magnetic field, where the relativistic effects are not dominating, the emitted cyclotron frequency is proportional to the magnetic field magnitude $\omega_c = \omega_c(B)$. The fact that in tokamaks the toroidal magnetic field B_T changes with $1/R$ can be used for an electron temperature measurement with a good spatial and temporal resolution. To ensure a transition of the magnetic field along the antenna line of sight, these measurements are mostly realised from the HFS or LFS of tokamak. We talk about the horizontally situated ECE diagnostics (H-ECE).

3.5.1 Suprathermal ECE

The electron cyclotron diagnostic system can be used to detect the presence of non-thermal electrons. In ITER, for example, the oblique view that is sensitive to a distortions in the electron momentum distribution near the average thermal momentum is planned [22]. It will be used in the comparison with the ECE measurement in the radial view. Antenna placed on the HFS can also observe down-shifted radiation of suprathermal electrons without absorption at the thermal resonance what could happen in the LFS case.

Experiments were made in a similar way for example on TEXT-U [23], TFTR [24], TCV [25] and DIII-D [26]. None of them has investigated the electron cyclotron emission of the runaway electron population. In this thesis we will explain another technique of the non-thermal electron cyclotron emission measurement where the receiver is placed vertically.

It is possible to restrain the influence of the varying magnetic field in (3.48) via a vertically positioned antenna (**V-ECE**). The toroidal magnetic induction value becomes approximately constant along the line of sight. Thus, the resonance condition depends only on the velocity. In such a situation with neglecting the Doppler shift, the emission at a particular frequency (ω) for a particular cyclotron harmonic (n) occurs only from the electrons satisfying the resonance condition

$$\frac{\omega}{n \cdot \omega_{ce}} = \sqrt{1 - \left(\frac{v_{\parallel}}{c}\right)^2 - \left(\frac{v_{\perp}}{c}\right)^2}, \quad (3.49)$$

where v_{\parallel} and v_{\perp} denote the velocities parallel and perpendicular to the toroidal magnetic field \mathbf{B}_T in tokamak. **This condition gives us a one-to-one relationship between the frequency and the electron energy.** As a result, one can diagnose the density and the velocity anisotropy of the electrons as a function of the energy at the expense of returning to a chord-averaged measurement [21]. The purpose of this measurement is the fact that the presence of a suprathermal population strongly affects the magnitude and the spatial location of the wave absorption.

Unfortunately, the antenna divergence is not negligible in many cases and \mathbf{B}_0 is not constant and it has a poloidal component, so the Doppler effect has to be taken into account. The equation (3.49) becomes

$$\frac{\omega(c - N_{\parallel}v_{\parallel})}{n \cdot \omega_{ce}c} = \sqrt{1 - \left(\frac{v_{\parallel}}{c}\right)^2 - \left(\frac{v_{\perp}}{c}\right)^2}. \quad (3.50)$$

This entails a complication into the relation between the frequency and electron energy. Only the emission from certain velocity phase space (v_{\parallel} , v_{\perp}) fulfils the condition (3.50).

Non-thermal electrons change the cyclotron emission spectra distinctly from the one in Figure 3.2, what can be seen in Figure 3.3. Vital practical requirement for the RE measurement is to avoid detecting multiple-reflected waves from the tokamak wall. In the analysis of the measured electron energy, a non-Maxwellian distribution function from other diagnostics or simulation code has to be utilized. For the exact value of the parallel optical index, we need to count the optical depth, the probability of reflections and the wave propagation in plasma. It is necessary to use the ray tracing calculations.

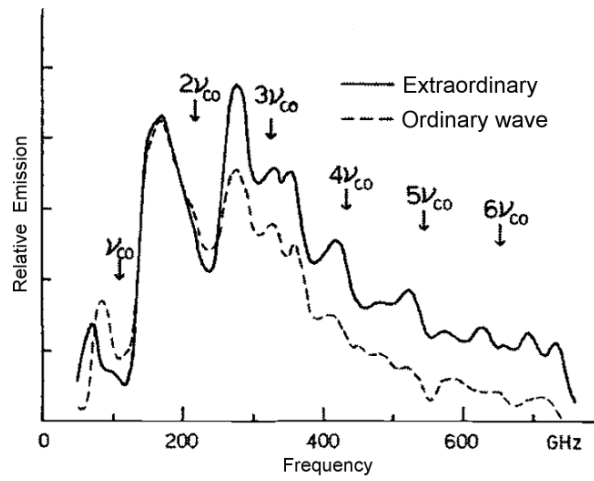


Figure 3.3: Typical cyclotron emission spectra when significant nonthermal components exist in the electron distribution [21].

3.6 Ray Tracing

Tokamak plasmas are in fact inhomogeneous. In this section, the geometrical optics for the wave propagation in non-homogeneous plasmas will be reviewed. The beam is considered as composed of independent rays, each propagating along the trajectory where the local dispersion relation is satisfied everywhere.

This approximation provides an elegant technique for accounting refractive effects in inhomogeneous plasmas, and plays an important role in the interpretation of measurements using electromagnetic waves [14]. In a weakly inhomogeneous plasma, properties of the medium vary in space and time. The relative change is small compared to the wavelength. As in the case of a homogeneous plasma, a non-trivial solution condition of the wave equation results in a local dispersion relation

$$\omega = \omega(\mathbf{k}, \mathbf{r}, t). \quad (3.51)$$

The ray equations then can be written in the canonical form [14]

$$\begin{aligned}\frac{d\mathbf{r}}{dt} &= \nabla_{\mathbf{k}}\omega, \\ \frac{d\mathbf{k}}{dt} &= -\nabla_{\mathbf{r}}\omega,\end{aligned}\tag{3.52}$$

with ω in the role of the Hamiltonian we get

$$\frac{d\omega}{dt} = \frac{\partial\omega}{\partial t}.\tag{3.53}$$

In the case of a known dispersion relation $D(\omega, \mathbf{k}, \mathbf{r}, t) = 0$, these ray equations transform into

$$\begin{aligned}\frac{d\mathbf{r}}{dt} &= -\frac{\nabla_{\mathbf{k}}D}{\partial D/\partial\omega}, \\ \frac{d\mathbf{k}}{dt} &= \frac{\nabla_{\mathbf{r}}D}{\partial D/\partial\omega}.\end{aligned}\tag{3.54}$$

For such a medium, it is convenient to use the arc length s along the ray as the parameter and express the ray equations [16][17] in the form

$$\begin{aligned}\frac{d\mathbf{r}}{ds} &= -\text{sgn}\left(\frac{\partial D}{\partial\omega}\right)\frac{\nabla_{\mathbf{k}}D}{|\nabla_{\mathbf{k}}D|}, \\ \frac{d\mathbf{k}}{ds} &= \text{sgn}\left(\frac{\partial D}{\partial\omega}\right)\frac{\nabla_{\mathbf{r}}D}{|\nabla_{\mathbf{k}}D|}.\end{aligned}\tag{3.55}$$

It is not possible to neglect the absorption and emission along the trajectory as a consequence of the kinetic effects. Anti-Hermitian components appear in the dielectric tensor and the solution of the dispersion relation is a complex vector $\mathbf{k} = \mathbf{k}_r + i\mathbf{k}_i$. We cogitate $|\mathbf{k}_r| \gg |\mathbf{k}_i|$ in the case of a plasma diagnostics. The hot plasma dispersion relation is still a fourth degree polynomial in the perpendicular component of the optical index N_{\perp}

$$D = \varepsilon_{11}N_{\perp}^4 + P = 0,\tag{3.56}$$

where D and ε_{11} are complex and P is a polynomial of third order in N_{\perp} . If N_{\perp} is finite and ε_{11} is nonzero the equation can be modified as

$$F \equiv \frac{D}{\varepsilon_{11}} = N_{\perp}^4 + \frac{P}{\varepsilon_{11}} = 0.\tag{3.57}$$

With respect to the condition $|\mathbf{k}_r| \gg |\mathbf{k}_i|$ we get $\text{Re}(P/\varepsilon_{11}) \gg \text{Im}(P/\varepsilon_{11})$ so

$$\begin{aligned}F(\omega, \mathbf{k}, \mathbf{r}, t) &\approx F_r(\omega, \mathbf{k}_r, \mathbf{r}, t) + iF_i(\omega, \mathbf{k}_r, \mathbf{r}, t) + i\mathbf{k}_i \cdot \nabla_{\mathbf{k}_r}F_r = 0, \\ F_r(\omega, \mathbf{k}_r, \mathbf{r}, t) &= 0, \\ \mathbf{k}_i \cdot \nabla_{\mathbf{k}_r}F_r &= -F_i(\omega, \mathbf{k}_r, \mathbf{r}, t).\end{aligned}\tag{3.58}$$

The second equation yields the ray equations similar to (3.54)

$$\begin{aligned}\frac{d\mathbf{r}}{dt} &= -\frac{\nabla_{\mathbf{k}_r} F_r}{\partial F_r / \partial \omega}, \\ \frac{d\mathbf{k}_r}{dt} &= \frac{\nabla_r F_r}{\partial F_r / \partial \omega},\end{aligned}\tag{3.59}$$

and the third one gives the equation for calculating the ray absorption between two points of a ray [14]

$$\int_{s_1}^{s_2} \mathbf{k}_i ds = \int_{s_1}^{s_2} \frac{|F_i|}{|\nabla_{\mathbf{k}_r} F_r|} ds.\tag{3.60}$$

It gets us to the radiation transfer. The equation for the radiation transfer used for the simulations is in the form

$$n_r \frac{d}{ds} \left[\frac{I_\omega}{n_r^2} \right] = \beta - \alpha I_\omega\tag{3.61}$$

with I_ω as the radiation intensity, α and β the absorption and emission coefficients and n_r the ray refractive index. As a result we get a parameter which is called the optical depth

$$\tau = \int \alpha ds.\tag{3.62}$$

It is crucial for a subsequent analysis of the simulations and ray tracing. **To secure the vital practical requirement, avoiding the detection of multiple reflections from the wall, a higher optical depth ($\tau > 1$) is needed** [21]. This requirement secures the conditions for the thermodynamic equilibrium where the Kirchoff's law applies as

$$I_\omega = \beta / \alpha.\tag{3.63}$$

In the presence of a significant amount of the non-thermal electrons, the Kirchoff's law no longer holds. The emission and absorption coefficients must be calculated separately.

On the other hand, if velocities have the Maxwell distribution and if the emission from a tokamak is considered as the black-body radiation, we can define its intensity as

$$I_\omega = \frac{\omega^2 T_e}{8\pi^3 c^2},\tag{3.64}$$

where the Rayleigh-Jeans approximation $\hbar\omega \ll k_B T_e$, the \hbar denotes the reduced Planck constant.

■ 3.6.1 SPECE Code

The SPECE code [27] was developed in the Istituto di Fisica del Plasma in Milan, Italy, for the analysis of the electron cyclotron emission. This code computes the solution of the equation of the radiation transfer along the ray trajectories in a general tokamak equilibrium, using the cold dispersion relation, while the absorption and emission coefficients are obtained as a solution of the relevant fully relativistic dispersion relation valid at a high electron temperature. The propagation is computed by solving the similar ray equations as (3.55) in the form

$$\frac{d\mathbf{r}}{ds} = -\frac{\partial D/\partial \mathbf{N}}{|\partial D/\partial \mathbf{N}|}, \quad \frac{d\mathbf{N}}{ds} = \frac{\partial D/\partial \mathbf{r}}{|\partial D/\partial \mathbf{N}|}, \quad (3.65)$$

where $D(\omega, \mathbf{N}, \mathbf{r}, t) = 0$ is the cold dispersion relation for the electron cyclotron waves with the frequency ω and the refractive index \mathbf{N} (3.24). SPECE uses (3.61) for computation the radiation transfer.

The magnetic equilibrium, plasma temperature and density profiles are given either analytically or numerically. Calculations can be done in a Maxwellian plasma or non-thermal plasma characterized by the distribution function given by a sum of drifting Maxwellian distributions. The actual antenna pattern is simulated by the means of a multi-ray calculation, using a set of m rays, uniformly distributed in the radial and angular directions with respect to the antenna axis. SPECE was utilized for an oblique electron cyclotron emission diagnostics at the JET tokamak and can be applied on other different devices including COMPASS or even ITER. [27]



Part II

Experimental Setup and Results

Chapter 4

Experimental Setup

4.1 COMPASS Tokamak

The COMPASS (from the COMPact ASSEMBly) tokamak is a compact-sized device developed in the Culham Science Center, England, in late 80's. It is a D-shaped tokamak capable of the high confinement mode, also called the H-mode, operation. COMPASS dimensions correspond to one tenth of ITER. Due to this two features it was offered by the European Commission and UKAEA to the Institute of Plasma Physics in Prague after the shut-down in Oxfordshire.

The main tokamak parameters are shown in Table 4.1

Major radius R	0.56 m
Minor radius a	0.23 m
Aspect ratio A	≈ 2.4
Plasma current I_p (max)	400 kA
Toroidal magnetic field B_T	0.9-1.5 T
Vacuum pressure p_0	10^{-6} Pa
Plasma shape	SND*, D, ellipse, circular
Elongation ϵ	1.8
Plasma duration t_p	≈ 500 ms
NBI 40 keV P_{NBI}	2×0.4 MW

*single-null divertor

Table 4.1: Basic parameters of the COMPASS tokamak.

The physics research programme on the COMPASS tokamak includes mainly studies of edge plasma, diagnostic system development, H-mode physics, MHD equilibrium and instabilities and runaway electrons. The runaway electron experiments are conducted under the MST1 (Medium Size Tokamaks) project of the EUROfusion, the coordinating organisation of the European fusion research centres.

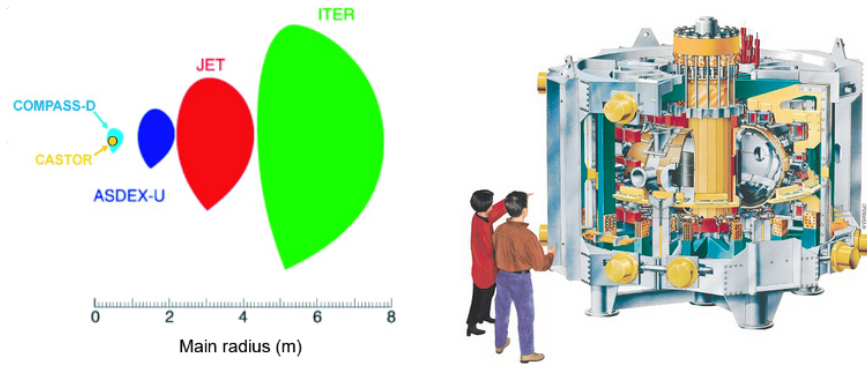


Figure 4.1: Scale of some European tokamaks with the cross-section similar to ITER and a cutaway diagram of the COMPASS tokamak [28].

4.2 ECE/EBW Heterodyne Radiometer

The ECE/EBW heterodyne radiometer was utilized in COMPASS for the measurement of electron Bernstein mode waves (EBW) [29]. These are quasi-electrostatic EC modes, which do not suffer from the high-density limitations. They play an important role in a low magnetic field, high-density plasma, for example in spherical tokamaks and stellarators.

The radiometer consists of a separated front-end and a 16-channel intermediate frequency (IF) receiver with the bandwidth 1.5–15 GHz. Each channel has a second mixer stage, a digitally controlled built-in attenuator 0–30.5 dB in 0.5 steps, a power detector and a DC amplifier, which provides a linear output voltage of 0–10 V / DC–1 MHz and the bandwidth 850 MHz.

The system, shown in Figure 4.2, contains front-ends with the Ka-band (26.5–40 GHz) or the E-band divided into two subbands (60–74.5 GHz/76.5–90 GHz). The receiver uses a vertical perpendicular vacuum chamber port. Horn antenna with a teflon lens is placed behind a silicon port window as it is shown in Figure 4.3 and it is connected to the radiometer over the ~ 2.5 m waveguide. [29][30]

No calibration during these experiments was utilized. ...

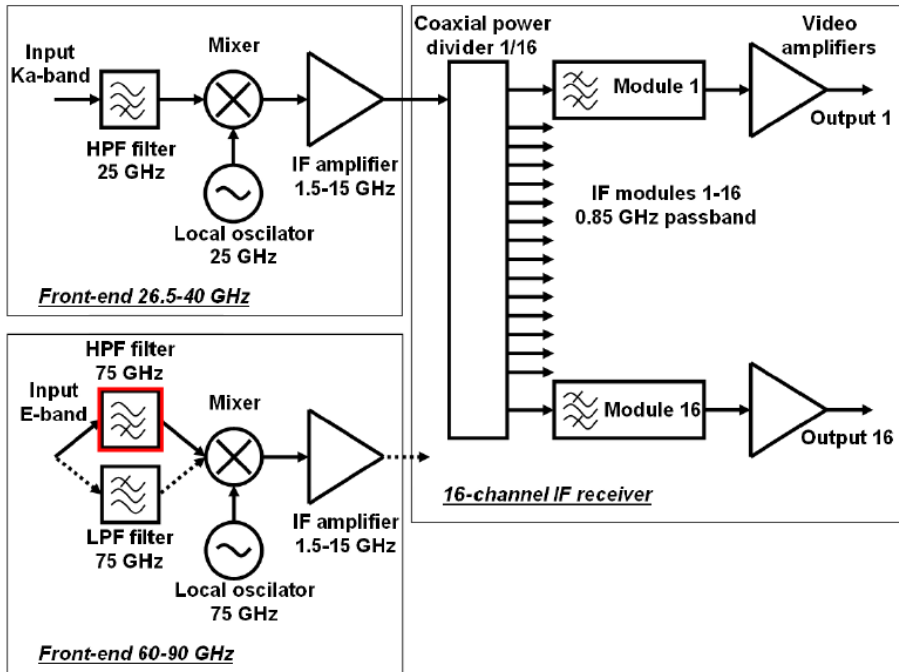


Figure 4.2: Block scheme of the ECE/EBW radiometer for COMPASS. Taken from [29].

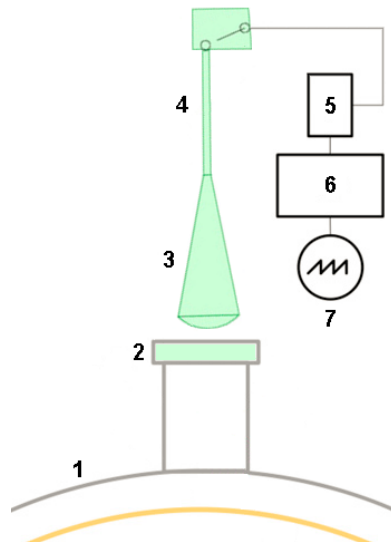


Figure 4.3: Scheme of the antenna setup. (1) COMPASS vessel; (2) vacuum silicon port window; (3) horn antenna; (4) waveguide; (5) front end; (6) IF receiver; (7) digital oscilloscope

Chapter 5

Simulations and Calculations

5.1 Frequency Range and Energy Spectra

In this chapter the simulation results, which have been used for the final design of the diagnostics and for the data interpretation, will be presented. The first thing to be investigated is the presence of cutoffs. The cutoff frequencies (3.37) increase with the electron plasma frequency ω_{pe} , which is dependent on the electron density $\omega_{pe} \sim \sqrt{n_e}$. It is favourable to choose the front-end frequencies as high as possible to be able to measure in the highest possible plasma densities. In Table 5.1 the electron cutoff densities for $B = 1.15$ T, i. e. at the magnetic axis of the COMPASS tokamak during a typical discharge are shown. If the density value is below the shown number, the measured wave is not limited by the cutoff area anywhere during its propagation through the whole plasma. In the case of the Ka-band, in frequencies lower than 30 GHz, we find ourselves in the forbidden region of propagation under the right-hand cutoff. This band is therefore worthless for the measurement of the waves with X-mode polarization.

	ν [GHz]	n_{eO} [10^{19} m $^{-3}$]	n_{eX} [10^{19} m $^{-3}$]
Ka-band	26.5	0.87	—
	38.3	1.82	0.29
E1-band	61.7	4.72	2.26
	74.5	6.89	3.91
E2-band	76.5	7.26	4.21
	88.3	9.67	6.15

Table 5.1: Cutoff electron densities of the O-mode (n_{eO}) and X-mode (n_{eX}) for the given front-end boundary frequencies ν in the plasma centre.

The most advantageous option is to choose the E2-band with the highest frequencies. **It is possible to measure the O-mode and X-mode waves at frequencies not limited by cutoffs in the case of low-density discharges, which are conducted on the COMPASS tokamak during runaway electron campaigns.** These discharges are characterised by the line-averaged electron density \bar{n}_e in the range $1 - 3 \cdot 10^{19}$ m $^{-3}$.

The electron kinetic energies (momenta) as well as the velocity phase space which fulfil the resonance condition can be determined from the range of frequencies with the use of equation (3.50). As it was mentioned earlier, the emitted cyclotron frequency is down-shifted in connection with reaching relativistic velocities. Along the line of constant magnetic field $B = 1.15$ T the cyclotron frequency has value $\nu_{ce} = 32.2$ GHz. It yields the fact that it is possible to measure the down-shifted radiation from the third and higher harmonic cyclotron frequency. Figure 5.1 and Figure 5.2 show the contour in the velocity phase space (\triangle) for the resonance condition and the kinetic energy (\bullet) relevant to the plotted point of the velocity phase space for 3rd harmonic frequency. The emission from the 4th and 5th harmonic frequencies has fairly weaker emission.

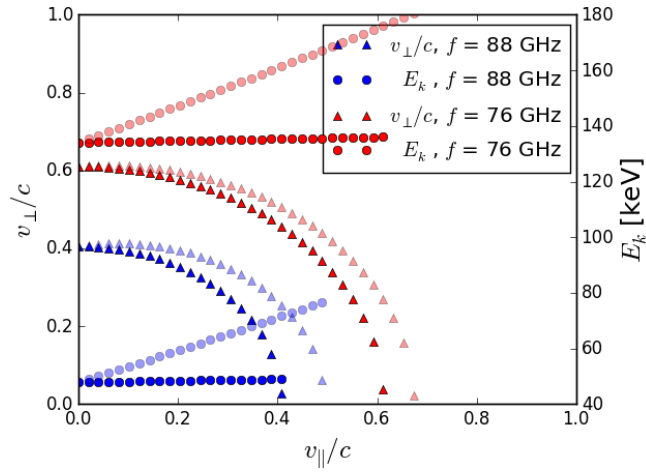


Figure 5.1: Solution of the resonance condition (3.50) with the value of the electron kinetic energy E_k for emission from the 3rd harmonic for the boundary E2-band frequencies. *Rich colour:* $N_{||} = 0.005$; *Pale colour:* $N_{||} = 0.1$.

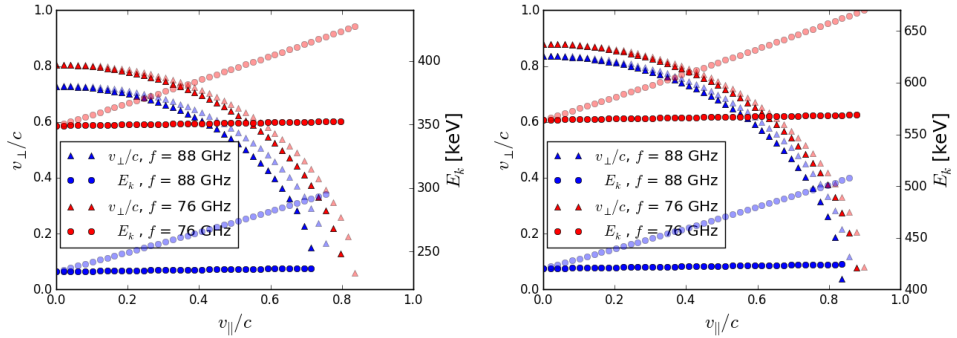


Figure 5.2: Solution of the resonance condition (3.50) with the value of the electron kinetic energy E_k for emission from the 4th (left) and 5th (right) harmonic for the boundary E2-band frequencies. *Rich colour:* $N_{||} = 0.005$; *Pale colour:* $N_{||} = 0.1$.

The later given ray-tracing simulations yields the value $N_{||} = 0.005$. From a brief look at the shown figures, we are able to determine the electron energies in resonance with the E2-band frequencies. This is the energy of **50 – 140 keV** (respectively 230 – 350 keV and 420 – 570 keV from higher harmonics).

Therefore, the low-energy REs with the parallel velocities above 0.4 c can be investigated. We can call the electrons in this phase space "runaway" because of the critical velocity maximum (2.7) in the V-ECE experiments ($n_{e,\max} = 4.2 \cdot 10^{19} \text{ m}^{-3}$, $U_{\text{loop}} = 0.7 \text{ V}$, $\ln \Lambda = 13$) which is $v_c = 0.37 \text{ c}$. It corresponds to the kinetic energy $E_{\text{ck}} = 36 \text{ keV}$. It is essential to keep in mind that the higher harmonic used the lower radiation intensity emitted as shown in Figure 3.3.

5.2 Optical Depth

The third thing to investigate is the wave mode suitability for the measurement, i. e. optical depth values for the O-mode and X-mode. In a Maxwellian plasma there is a low number of the resonant electrons, therefore neither absorption nor emission occurs in the centre along the line of constant magnetic field B_0 in the measured frequency range 76.5 – 88.3 GHz. This fact is favourable for the measurement of the runaway electrons. It is necessary to add a non-thermal component into the simulation to increase the absorption coefficient and then the optical depth. The simplest way is to use a bi-Maxwellian plasma. In the SPECE code, the added non-thermal component is characterized by the velocity $u_{\max} = p/mc$ at the end of the tail plateau, by the temperature T_{tail} and distribution function in space and normalised magnetic flux coordinate

$$\eta = \frac{n_{e,\text{tail}}}{n_{e,\text{bulk}}} = \eta_0 \exp \left[- \left(\frac{\psi - \psi_0}{\psi_c} \right)^2 \right]. \quad (5.1)$$

Values of dimensionless parameter η_0 and magnetic flux coordinates ψ_0 and ψ_c have to be chosen. For the sake of simplicity, assume a runaway electron presence only in the center of the plasma. This assumption gives $\psi_0 = 0$. The width of the spatial distribution function is chosen as $\psi_c = 0.1$. A number of runaways can be roughly estimated from the measured RE current I_{RE} as

$$N_{\text{RE}} = \frac{2\pi R I_{\text{RE}}}{ec\pi a^2}$$

In COMPASS, the runaways constitute at most a thousandth of all electrons present in the plasma in a low-density discharge. This gives us the simplified equation

$$\begin{aligned} N_{\text{RE}} &= \int_{\psi=0}^{\psi=1} n_{e,\text{tail}} \cdot dV = n_{e,\text{bulk}} \sum_{\psi} \eta \Delta V_{\psi} = \\ &= n_{e,\text{bulk}} \eta_0 \sum_{\psi} \exp \left[- (10 \cdot \psi)^2 \right] \Delta V_{\psi} \approx 1 \cdot 10^{16} \end{aligned}$$

and the solution

$$\eta_0 = \frac{1 \cdot 10^{16}}{n_{e,\text{bulk}} \cdot \sum_{\psi} \exp \left[- (10 \cdot \psi)^2 \right] \Delta V_{\psi}}. \quad (5.2)$$

Together with the n_e and T_e profiles from the shot #13127 and the choice of $u_{\max} = 0.4$ and $T_{\text{tail}} = 60$ keV to fit the resonant parameters from Figure 5.1 we get $\eta_0 = 0.015$. The density profile was multiplied by a constant to get a profile with maximal density in the center of the plasma $n_{e,\max} = 3 \cdot 10^{19} \text{ m}^{-3}$ and secure no limitations by the cutoffs. The profiles are in Figure 5.3.

The optical depth can now be evaluated for the O-mode and X-mode. This particular simulation can be seen in Figure 5.4. Values of the optical depth for the X-mode are 20 times higher than for the O-mode.

During the evaluation of various simulations this difference between values of the optical depth stayed almost the same. As it was mentioned earlier, the goal is to prevent the detection of waves reflected from the tokamak wall. In the case of $\tau > 1$ the reflections are negligible but unfortunately parameters of the plasma and the available radiometer on COMPASS do not provide this suitable condition. The choice of the X-mode polarization is still advantageous, however the data analysis is going to be considerably onerous.

For the V-ECE measurements of the runaway electrons the E2-band was selected with the frequency range 76.5 – 88.3 GHz with O/X-mode polarization. At this moment it is possible to check the trajectories dependent on the cutoff presence, as shown in Figure 5.6. The propagation and reflection of the beam is displayed.

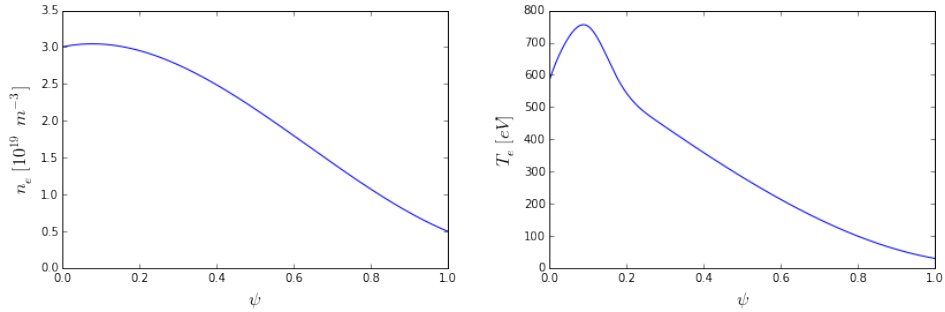


Figure 5.3: Used electron density n_e and temperature T_e profiles from TS dependent on the normalised poloidal magnetic flux ψ .

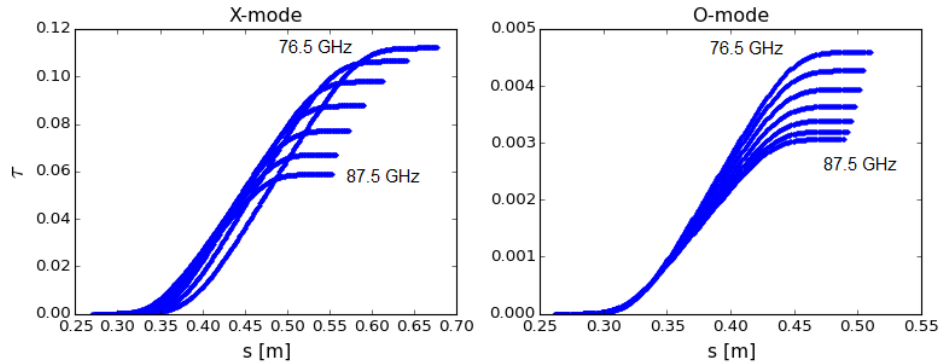


Figure 5.4: Values of the optical depth τ dependent on the ray path length s for both O-mode and X-mode for odd E2-band channels.

If we take the detection of the reflected emission into account, the measured spectrum of energies can be broadened due to the varying magnetic field. The measured energies could be potentially in the range 0 – 500 keV from the 3rd harmonic. Hence, there is a possibility to measure the thermal emission. Nevertheless, the reflected waves can lose some of their intensity. Also, the vessel shape of COMPASS is not significantly suitable for the detection of the reflected emission by a diagnostics placed in a vertical port. That is why we will consider this broad spectrum possible but not necessarily measurable.

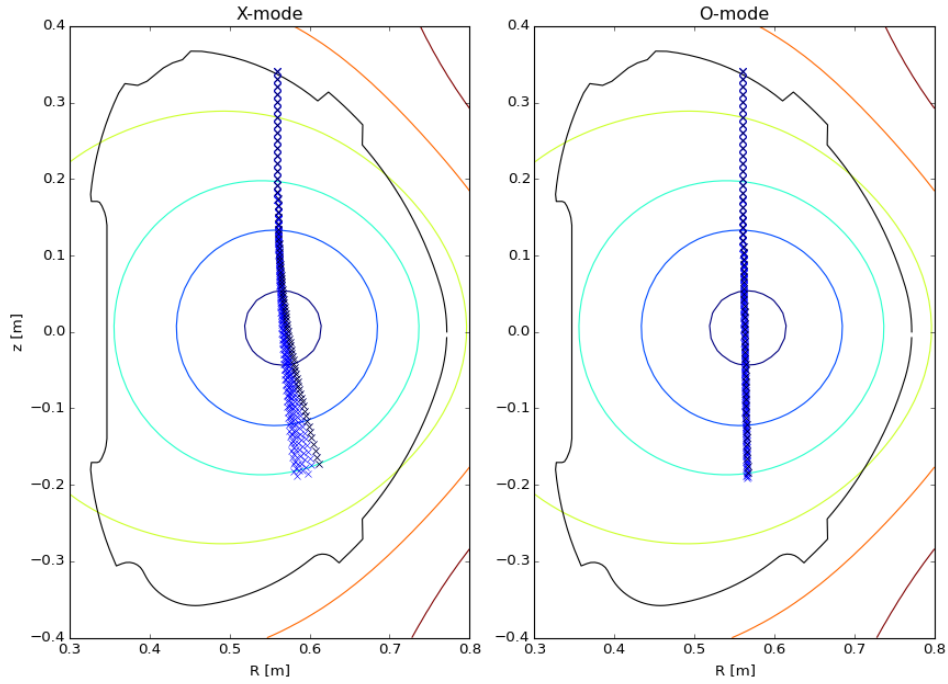


Figure 5.5: Poloidal view of the trajectories of X-mode and O-mode rays in the COMPASS tokamak, profiles from Figure 5.3, frequencies 76–88 GHz, $B = 1.15$ T.

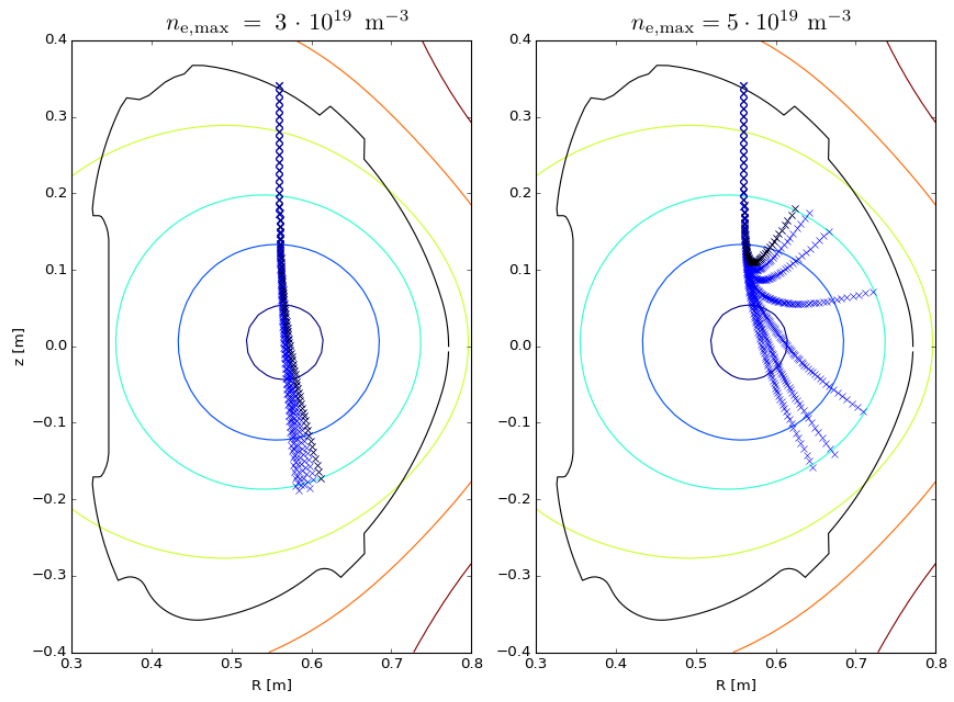


Figure 5.6: Poloidal view of the trajectories of the X-mode ray with the maximum electron density in the center of the plasma $n_{e,\max} = 3 \cdot 10^{19} \text{ m}^{-3}$ ($\bar{n}_e = 1.75 \cdot 10^{19} \text{ m}^{-3}$) and $n_{e,\max} = 5 \cdot 10^{19} \text{ m}^{-3}$ ($\bar{n}_e = 3 \cdot 10^{19} \text{ m}^{-3}$), $B = 1.15 \text{ T}$.

Chapter 6

Measurements and Data Analysis

The characteristics of the discharge in the COMPASS tokamak together with the measured data will be presented. The data analysis will be mainly focused on confirmation of the simulation results. It is necessary to prove that the measured V-ECE is related to the emission of suprathermal electrons.

All the measurements were realised within the runaway electron campaigns in COMPASS which are a part of the European research. The RE research group works in cooperation with the Medium-Size Tokamak Task Force (MST1) - Topic 8. Its goal is to demonstrate the post-disruption runaway electron beam control, extend the understanding of the runaway electron physics and their interaction with an injected gas and magnetic perturbation. This research is also supported by the Czech Science Foundation Project No. GA18-02482S.

Only the RE experiments in COMPASS reach a satisfactory low values of the electron density. Thus, the cutoff condition for the both O-mode and X-mode is not fulfilled, which is crucial for the electron cyclotron measurements.

The RE campaign studies include:

- Runaway electron presence in the flattop phase of low-density discharges.
- Disruptions with the RE beam generation using a high Z impurity massive gas injection (MGI) to terminate the thermal plasma.
- Mitigation techniques of the generated RE beam.
- Interaction of REs with with intrinsic magnetohydrodynamic (MHD) instabilities and also externally applied resonant magnetic perturbations (RMPs).

In the first parts of this chapter, the discharges focused on the flat-top runaways will be shown. The discharges used in this thesis are from the RE campaigns that were conducted in 12/2016, 06/2017 and 11/2017. [31]

6.1 Discharge Characteristics

Firstly, it is appropriate to present the discharge characteristics in COMPASS. The typical value of the magnetic field in the centre of the vacuum vessel is $B = 1.15$ T.

A discharge begins by ramping up the toroidal magnetic field at $t = 0$ ms (not shown in the figure). Phases of a discharge are marked in Figure 6.1. At 958 ms a neutral gas breaks down to form the plasma which is ionized and heated in the current ramp-up phase. When the plasma current reaches the required value, the feedback system maintains the requested conditions, this is called the flat-top phase. The termination of the plasma follows in the ramp-down phase where the current is reduced slowly. Discharge can end also by a disruption, but it is in most cases not a preferred option since this event has bad effects on the tokamak condition.

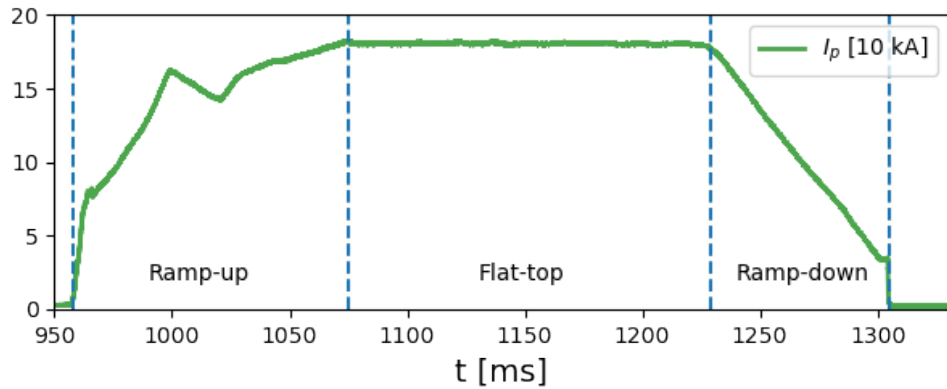


Figure 6.1: Plasma current evolution in a tokamak COMPASS discharge. Shot #13086.

The main quantities used in this thesis include the plasma current I_p , loop voltage U_{loop} and the electron density n_e . Signal from the V-ECE radiometer will be compared with other RE diagnostics implemented at this tokamak (See section 2.2) such as a hard X-ray scintillator (HXR), a shielded HXR detector and high-speed visible light cameras.

In the following text of this thesis, if it is not said otherwise, the discussed and shown V-ECE signal corresponds to the signal from the channel 1 (ch1) with the measured frequency of 76.5 GHz and the X-mode configuration. In the same manner the magnetic field at the magnetic axis is 1.15 T.

In general, some of the used signals have a considerable level of noise. Thus, a smoothed signal is convenient to plot in figures. For the sake of clarity, the rich coloured signal is the smoothed one while the pale signal is the raw signal measured by the given diagnostics.

6.2 Emission Source Verification

The first thing that has been investigated is the V-ECE signal from a high-density discharge without a significant runaway electron presence. This experiment is able to ascertain the existence of a spurious signal. Discharge with the density higher than the cutoff condition is chosen and shown in Figure 6.2. In the case of the line-averaged density $\bar{n}_e = 5 \cdot 10^{19} \text{ m}^{-3}$, only a noise level signal was measured during the flat-top phase of this discharge which means that **unwanted signal did not appear**.

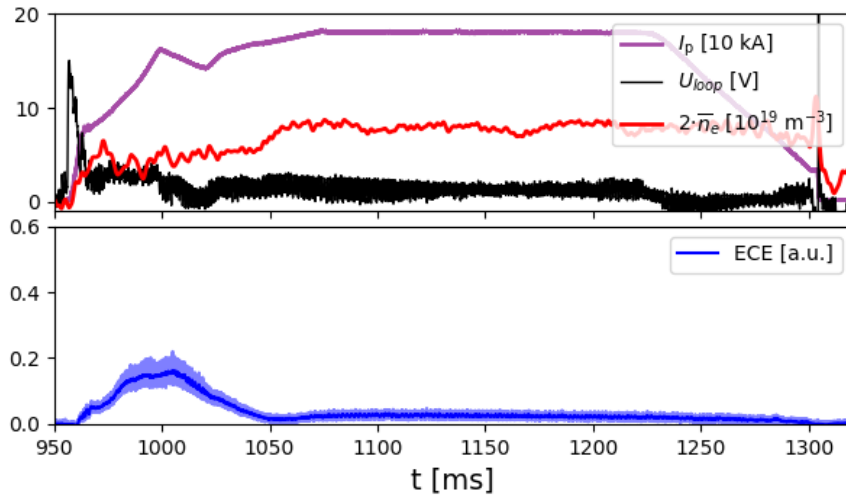


Figure 6.2: Plasma current I_p , loop voltage U_{loop} , line-averaged density \bar{n}_e and V-ECE signal of the shot #13086. (X,ch1)

Now, we can focus on experiments with densities below the cutoff condition i. e. discharges with the line-averaged density $\bar{n}_e < 2.6 \cdot 10^{19} \text{ m}^{-3}$. In these experiments, various V-ECE signals occur. Firstly, it has to be verified that the suprathermal electrons are the source of the measured emission. As an indicator of the runaway presence, the HXR diagnostics can be used. The main disadvantage of the HXR scintillation detector is a low threshold of the saturation. The HXR scintillator signal cannot tell the difference between the runaway electron quantities in the situation of a sufficient number of these particles. In this situation, the shielded HXR detection can be used as a complementary indicator. The lead-shielded HXR detector measures primarily a multi-MeV HXR. It can detect some photon-neutrons as well. Both HXR diagnostics measure the RE losses.

It is necessary to investigate the possibility of the thermal emission measurement. In the tokamak plasma with $B = 1.15 \text{ T}$, two thermal emission regions occur. In these regions the non-relativistic thermal electrons fulfil the cold EC resonance condition (3.38 for $\gamma \rightarrow 1$). As it is seen in Figure 6.3, there is a thermal region in the HFS from the 2nd harmonic and in the LFS from the 3rd harmonic. The possibility of a detection of the reflected emission has been discussed therefore a thermal emission measurement is still feasible.

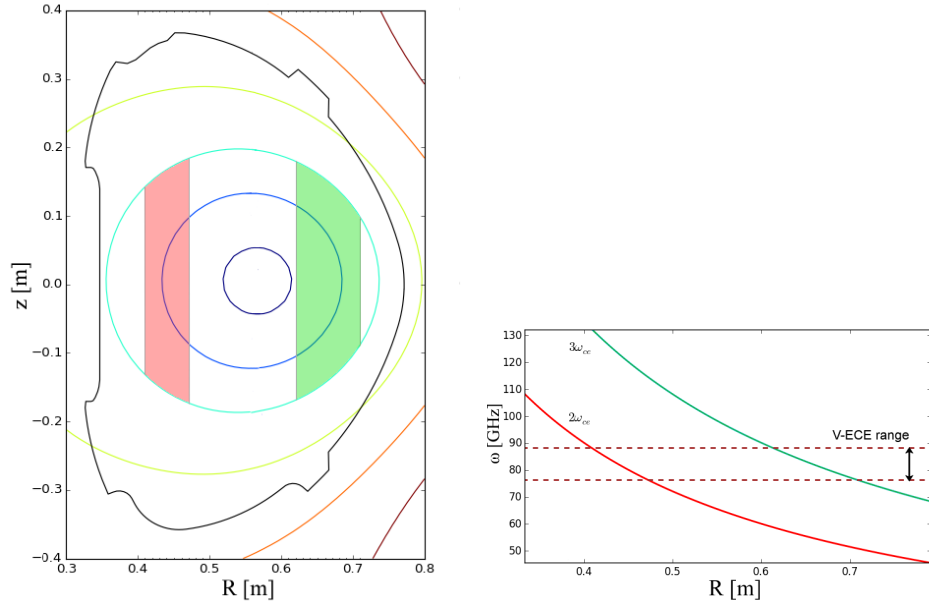


Figure 6.3: *Left:* Thermal ECE regions in plasma. Red: 2nd harmonic; Green: 3rd harmonic. *Right:* EC frequency profiles for $B = 1.15$ T.

The shot #14574 will serve us as a counterexample. It is a discharge with the density ramp-down. In the Figure 6.4, there is a comparison of the electron temperature T_e measurement ($R = 0.66$ m) done by the Thomson scattering (TS) system together with the V-ECE signal from the radiometer. **No dependence of the V-ECE signal on the electron temperature has been found** in any of the approximately 300 studied discharges. The discharges with higher magnetic fields, where the thermal region is placed in the centre of the plasma, are discussed in section 6.4.

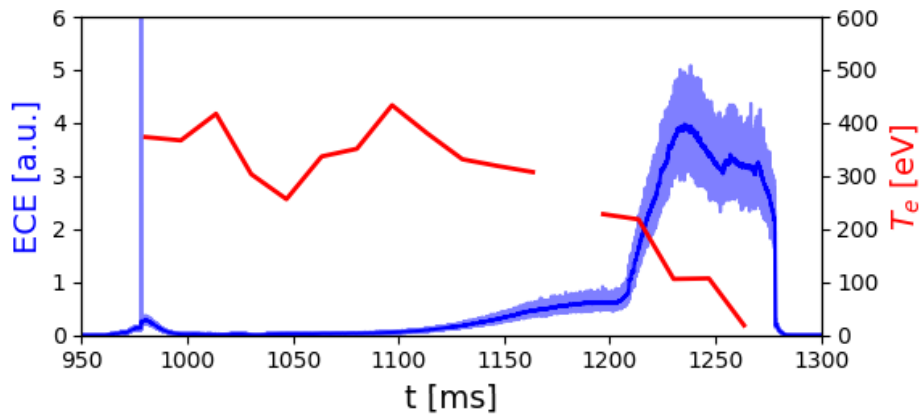


Figure 6.4: Comparison of the V-ECE signal (*blue*) with the T_e from the Thomson scattering (*red*) in the shot #14574. (X,ch1)

We have found no spurious signal or unwanted detection of the thermal emission. It remains unsolved whether the V-ECE measurement in COMPASS really comes from suprathermal electrons i.e. low-energy runaways. Comparison of the V-ECE diagnostics with the HXR detection was made and it is shown in Figure 6.5. The figure shows the comparison of three low-density flat-top shots 14468, 14469 and 14471. Each shot contains a different number of the REs, which is visible on the diagnostics in the fourth plot. There is similar HXR signal (3rd plot) due to the saturation of the HXR scintillation detector in the shots 14469 and 14471.

This is a strong indication that low-energy runaways are the source of the detected electron cyclotron signal. The results from this collation are in a good agreement with other measurements of the International Tokamak Physics Activity (ITPA) joint experiment group [10]. This experiment is similar to the one performed in TEXTOR. There were measurements of the RE threshold condition, where a significant number of REs occurs, as a function of the electron density. The same threshold occurs in COMPASS too and it can be estimated as $\bar{n}_e = 1.6 \cdot 10^{19} \text{ m}^{-3}$.

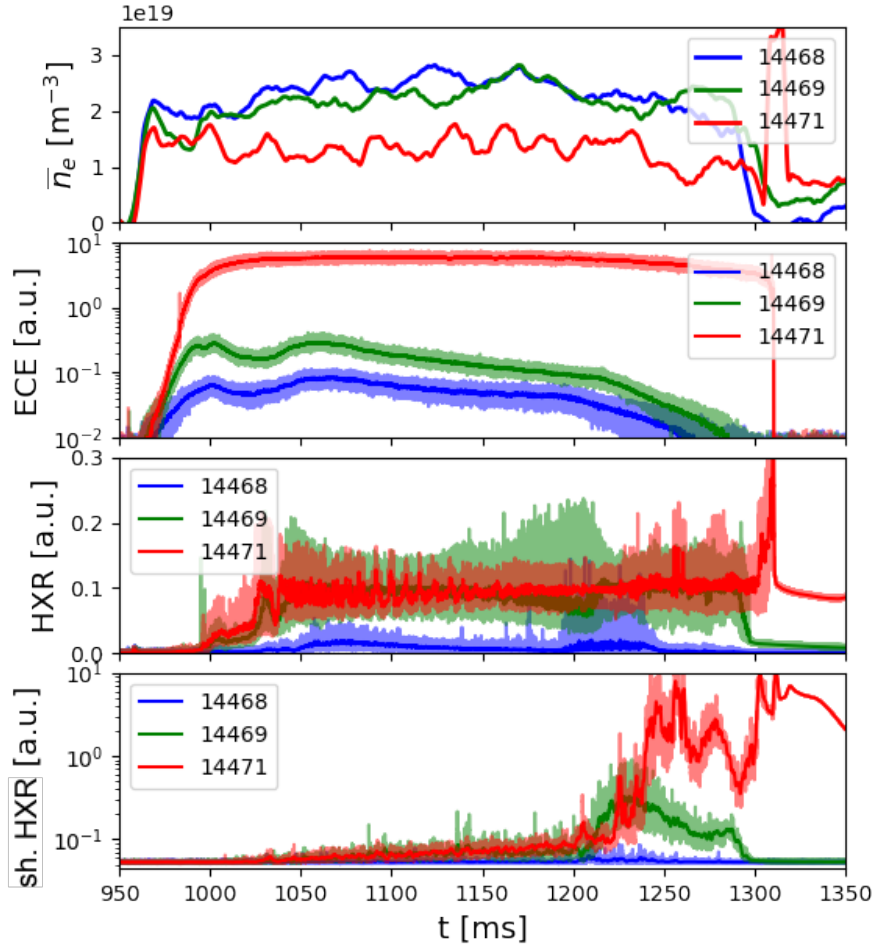


Figure 6.5: Comparison of the electron density, V-ECE and (shielded) HXR measurement from the shots 14468, 14469 and 14471. (X,ch5)

Refraction of emitted waves occurs at different densities. We have to investigate how the density change affects the V-ECE signal. The detection of the electron cyclotron emission of suprathermal electrons is not fully dependent on the electron density, unless we reach the cutoff densities. However, the electron density takes place in the runaway electron generation physics, especially in the primary Dreicer mechanism (2.6). The electric field E in the tokamak plasma does not vary during the discharge #14474, but the critical field E_c increases. The primary generation mechanism weakens with the decreasing ratio E/E_c this means that a lower number of electrons is accelerated by the electric field. In the case of the low-energy suprathermal electron emission measurement, this decrease of the RE generation is observed. In general, the V-ECE signal is not a function of the density, even though the density affects the RE generation.

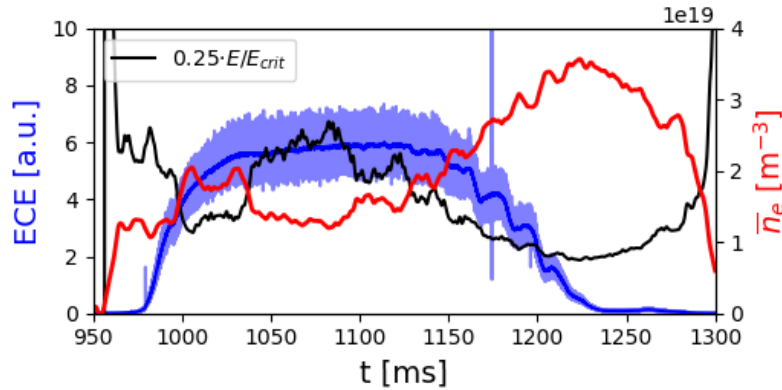


Figure 6.6: Comparison of the V-ECE signal with \bar{n}_e in the shot #14474. Shown signal of ch5 with measured frequency 80 GHz. (X,ch5)

6.3 O-mode/X-mode Comparison

A half of the discharges in the latter mentioned RE campaigns were performed with detection of the O-mode polarization i. e. with antenna rotated about 90° . Thanks to the measurements of both modes in the similar scenarios the comparison may be done. Even though the different waveguide components, such as bends, are used, this collation is useful.

Surprisingly, the measurements showed very similar results. For example in Figure 6.7, the comparison of X/O mode measurement in density ramp-down scenario is provided. The results are in a contradiction with ray-tracing and calculations of the optical depth in the section 5.2. The ratio between the intensities of the X-mode and O-mode emission should be the same as the ratio of the optical depths $\tau_X/\tau_O \approx 20$. We do not observe this phenomenon. The explanation of this is probably hidden in the detection of reflected waves. The V-ECE radiometer may detect a depolarized emission reflected from the tokamak first wall. If this is the case, the calculated energy spectra Figure 5.1 slightly broadens. We are still able to measure mainly low-energy REs.

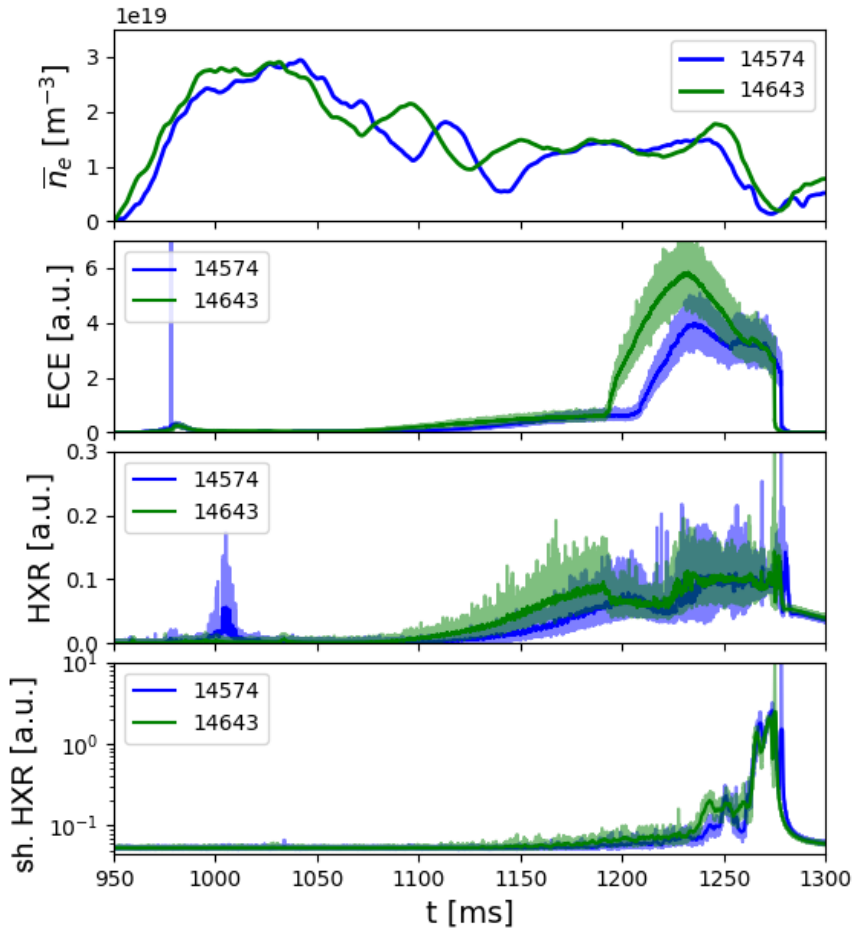


Figure 6.7: Comparison of the X-mode (#14574) and O-mode (#14643) electron density, V-ECE and (shielded) HXR measurement. (XO,ch1)

6.4 High B discharges

Experiments with a higher magnetic field were performed. The value of the magnetic field was up to $B = 1.5$ T at the magnetic axis of the tokamak. In that case, the region of the 2nd harmonic thermal emission shifts towards the LFS into the exact centre of the tokamak vessel. Thus, it appears right in the line of sight of V-ECE diagnostics.

Comparison of the standard B discharges with the high field discharges should clarify the question of the detection of the thermal emission. In this case we do not have to rely on the detection of reflected waves. An example of such a comparison is in Figure 6.8. We do not see any significant differences between V-ECE signals in these two scenarios. Even on the individual channels we do not observe any conspicuous differences. The emission intensity from the REs is probably much higher than the thermal emission intensity.

The fact that we should observe some disparity according to the theory will be investigated in future.

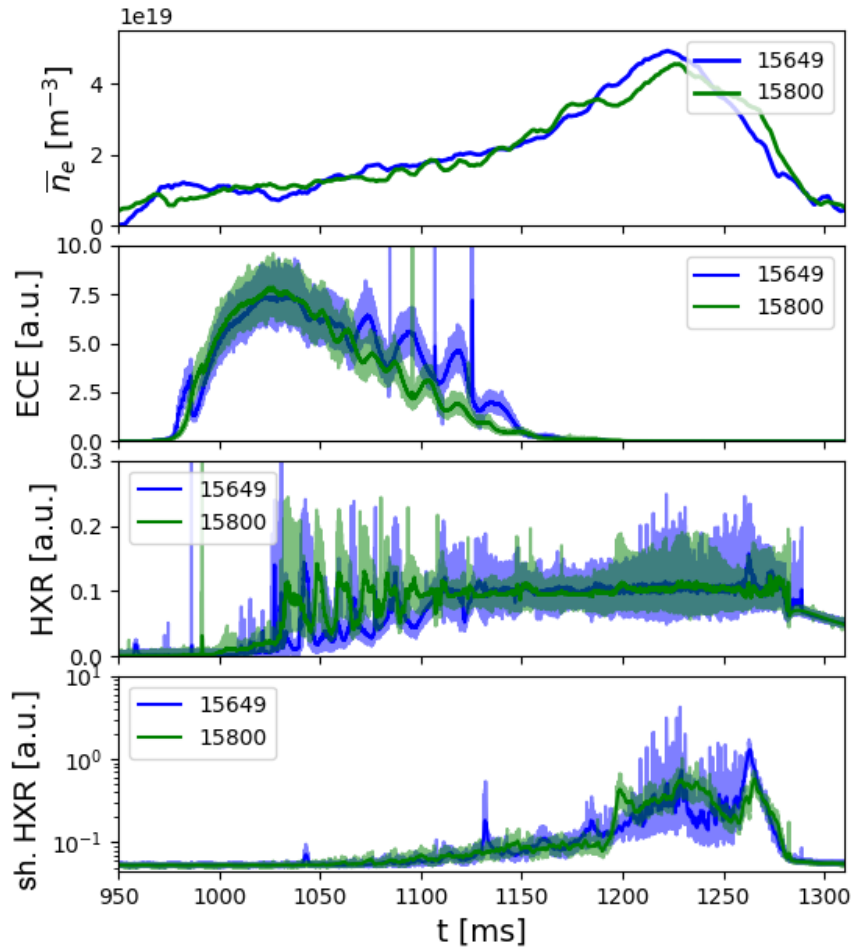


Figure 6.8: Comparison of the electron density, V-ECE and (shielded) HXR measurement from the ordinary $B = 1.15$ T (#15649) and high field $B = 1.50$ T (#15800) discharge. (O,ch1)

6.5 Primary Generation Measurements

After the confirmation of the V-ECE signal source and other properties of the measurement, we are now prepared for a data analysis. It will be done mainly in terms of the primary runaway electron generation and the RE distribution function development during the flat-top phase of the low-density discharges.

Firstly, we will look at the generation of the so called runaway seed. It can be seen in Figure 6.9 in the second plot. The generation of the runaway seed occurs during the ramp-up phase of the discharge where there is a low density but a high U_{loop} i. e. the electric field E . In Figure 6.7, the density ramp-down experimental scenario with generation of the RE seed (#14574) is presented. The low-energy runaway population is to some extent terminated as shown by the 24ms delayed detection of the HXR. The REs are accelerated and collide with the tokamak first wall. It might seem that REs are fully mitigated by the high electron density ($\bar{n}_e = 3 \cdot 10^{19} \text{ m}^{-3}$) but

the opposite is true. Some part of the RE distribution function is confined for the whole duration of the discharge. Still, we can obtain the confinement time of the electrons which were actually lost from the plasma. By normalising and shifting the HXR signal, we get the confinement time circa 24 ms for this particular discharge scenario. The REs generated later and also created due to primary generation mechanism, i. e. by decreasing the critical electric field (2.6), are confined for the same period of time. The decrease of E_c is caused by the electron density ramp-down during flat-top phase. In the first plot we see higher density shot 13137 with constant RE generation and losses where the entering edge of the V-ECE and HXR signals is shifted by 18 ms. The confinement time is in general within the range 15 – 25 ms.

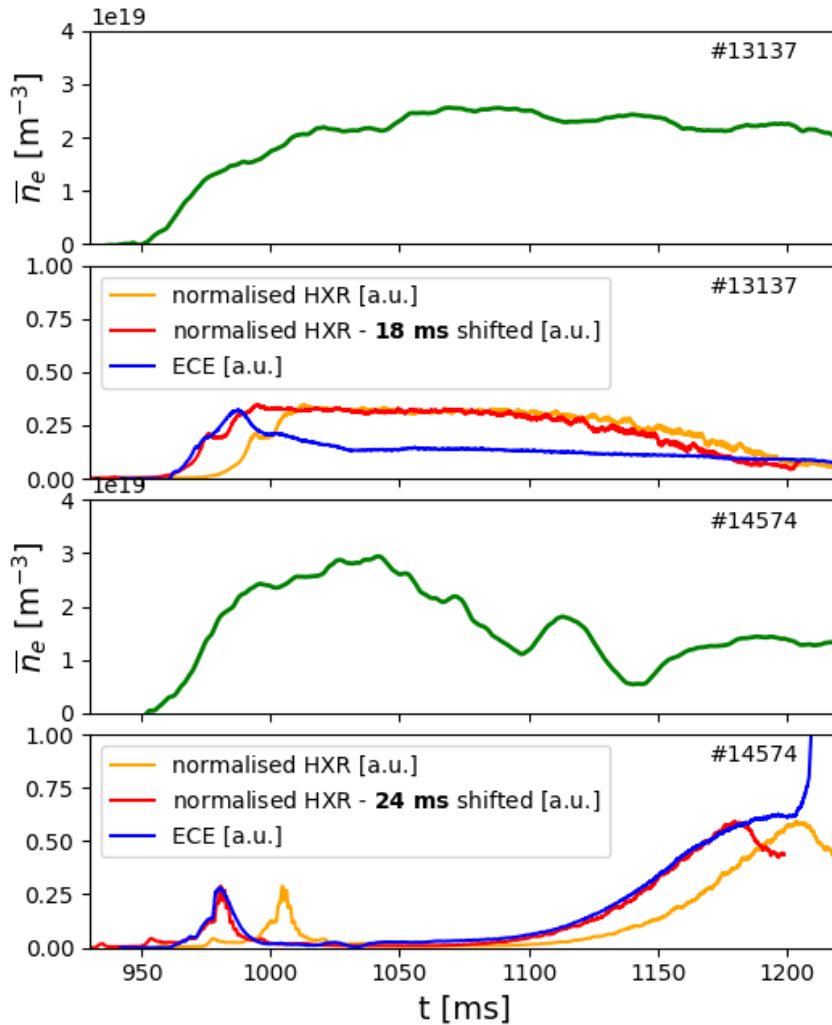


Figure 6.9: Correlation of smoothed HXR and V-ECE diagnostics for the shots 13137 and 14574. (X,ch1)

At the 1210 ms there is a steep increase of the V-ECE signal. Strong signal follows and it could be related to the density threshold discussed above (Figure 6.5). The threshold is around $\bar{n}_e = 1.5 \cdot 10^{19} \text{ m}^{-3}$ during the plasma

current flat-top in the density ramp-down scenario. It varies shot by shot due to a different runaway seed and electron density fluctuations. It is necessary to point out the fact that the interferometer installed on COMPASS cannot handle the measurement of densities below $\bar{n}_e = 1 \cdot 10^{19} \text{ m}^{-3}$. The steep increase of the V-ECE is probably also caused by the secondary avalanche mechanism (See subsection 2.1.3).

Let us have a deeper look at the critical electric field value E_c . The empirically determined RE thresholds were found not to agree with (2.6) in tokamaks. In COMPASS, a non-negligible number of runaways occurs only in the case of $E > 10 \cdot E_c$ and the threshold is even higher in some COMPASS discharge scenarios. We will define this value, based on previous research of the RE group [31], as $E_{\text{ctok}} = 12 \cdot E_c$. The V-ECE signal increase in Figure 6.7 happened in the flat-top phases of the discharges at $\bar{n}_e = 1.5 \cdot 10^{19} \text{ m}^{-3}$ and $U_{\text{loop}} = 0.7 \text{ V}$. This gives us the ratios

$$E/E_c = 17.5 \quad \text{and} \quad E/E_{\text{ctok}} = 1.46.$$

A runaway seed significantly influences the evolution of the RE presence within a discharge. The V-ECE diagnostics is able to record these connections what is shown in Figure 6.10. In the yellow rectangle, there is highlighted the difference between a shot with a lower initial RE seed and a shot with a larger initial RE seed. The primary generation in the shot 14642 is lower due to the higher electron density. Because of the missing the whole runaway population in the ramp-up phase of the discharge, we do not measure strong V-ECE signal neither the signal leap during the discharge. Thus, the HXR scintillator measures only the signal during the plasma termination at the end of the discharge. The case of the shot 14643 is the same as it was discussed earlier, it is ordinary discharge with the density ramp-down and a large RE population. It is worth mentioning that there are no initial RE losses detected by the HXR scintillator. However, the V-ECE signal leap occurs during the flat-top phase. This strong increase could be consequence of larger number of primary-generated REs. That could imply the confinement of a vast majority of the generated runaways of this initial seed. This could also indicate the influence of the secondary generation (avalanche) mechanism later in the discharge.

The V-ECE measurement provides information about the low-energy runaway electron presence especially about the primary generation at the beginning and in the flat-top phase of the discharge. It can be used as a routine diagnostics in the RE campaigns. Correlation of the measured frequencies (energies) could be delivered. For better understanding of the measured data and subsequent analysis, a comparison with simulations of the runaway physics (bounced-averaged kinetic electron simulator LUKE, fast tokamak transport simulator METIS) will be done. The analysis of the V-ECE measurements will be also very useful even in the case of the MGI (Ar, Ne) and RMP experimental scenarios. Some of the results will be briefly described further in next chapters.

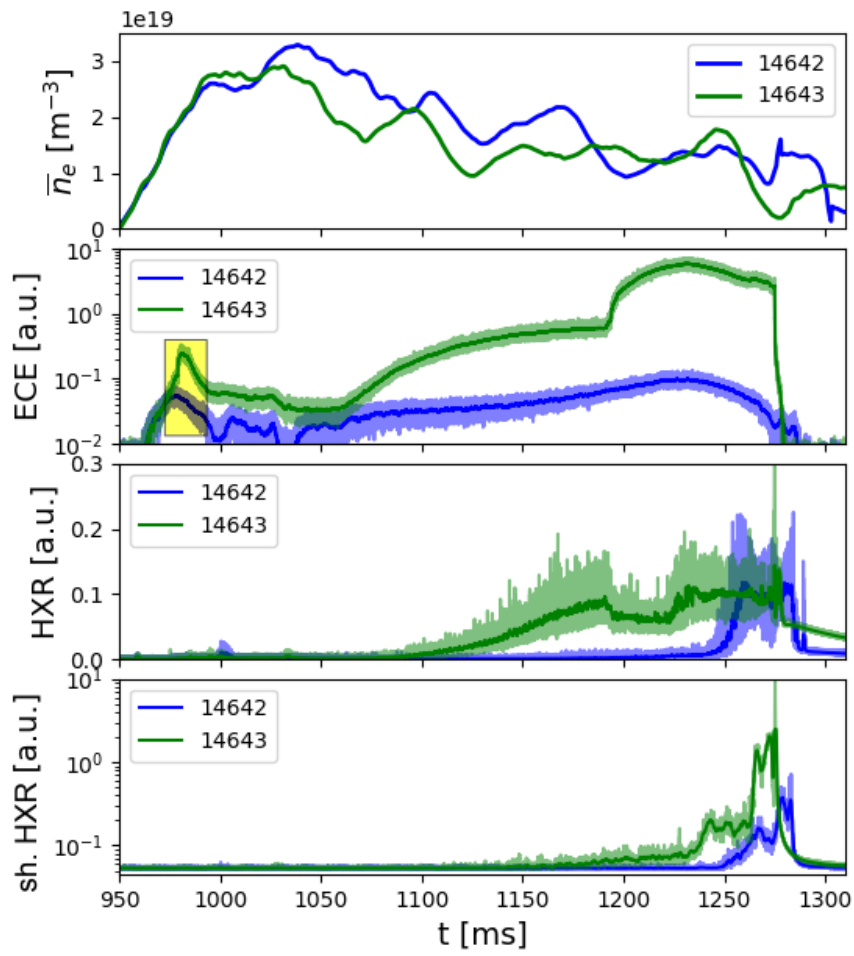


Figure 6.10: Comparison of the electron density, V-ECE and (shielded) HXR measurement from #14642 and #14643. Yellow rectangle highlights the runaway seed. (O,ch1)

6.6 Other RE Experiments

This chapter collects preliminary results of other experiments performed during RE campaigns in the last year.

6.6.1 Massive Gas Injection Experiments

A considerable amount of the experimental time was dedicated to massive gas injection (MGI) experiments. Most often, these experiments use high Z gas puffs, for example argon, into the ramp-up phase of a discharge. It causes the radiative disruption during which the fastest electrons are subject to the Dreicer and the hot-tail generation mechanism and a RE beam is created.

Two scenarios of the RE beam generation were observed. It can be seen in Figure 6.12. The argon gas puff reaches the vacuum vessel at 969 ms and a millisecond after that in the shot 15724 the current quench (CQ) occurs. From the V-ECE diagnostics we can estimate that before the CQ in this shot there was no initial RE population. At the CQ, magnetic surfaces gradually collapse and filamentary structures are visible by the RIS camera, see Figure 6.11. The filaments are captured also by the V-ECE in form of frequent peaks. In the Vlainic classification [32] we talk about the strong beam. The RE beam has a minimum time to form itself and the generation is rather turbulent.

The second type of the RE beam generation is observed in the discharge 15722. The formation of the REs started slightly before the argon puff has reached the vessel. The RE generation is not so turbulent, there are no collapsing magnetic surfaces. Due to the initial RE presence, the entire plasma current is carried by the RE beam. There is no current quench. The RIS camera sees a wide non-filamentary RE beam column. In the Vlainic classification we talk about the slow beam. The RE beam has a sufficient time to form itself and the generation is rather calm. The RE beam, which is generated in this way, is sustained in the tokamak for much longer. There are only high-energy runaways, which cause the lack of the V-ECE signal in a later stage of the beam from 970 ms till the end of the discharge. The differences between these scenarios seem to disappear in high B -field discharges.

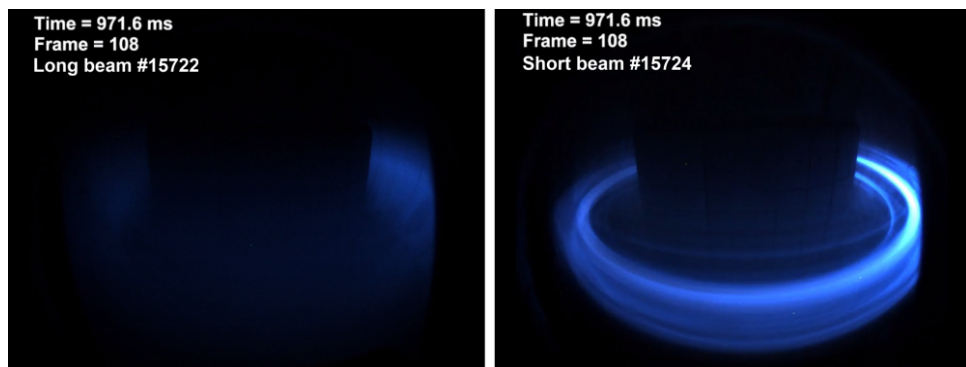


Figure 6.11: Pictures of the visible RIS camera from the discharge with the slow beam generation (#15722) and the strong beam generation (#15724).

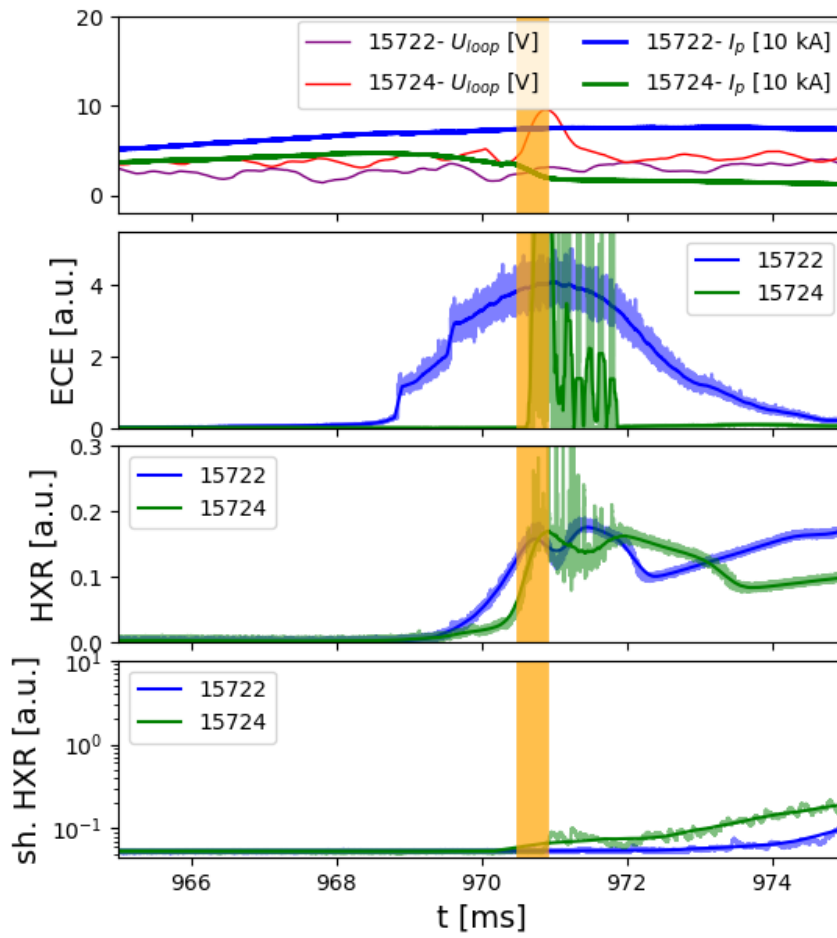


Figure 6.12: Comparison of the electron density, V-ECE and (shielded) HXR measurement from the shots with the slow beam generation (#15722) and the strong beam generation (#15724). Orange denotes the current quench. (O,ch1)

6.6.2 Resonant Magnetic Perturbations Experiments

One of the ways of mitigation the runaway electrons in large devices is by the reduction of their loss time. It could be achieved by the application of 3D error fields. Resonant magnetic perturbation coils (RMPs, typically saddle coils) are used for this purposes.

In the COMPASS tokamak during the RE campaigns there were used the LFS coils. In general, COMPASS is equipped with extensive RMP system including HFS coils. The system can generate RMPs in the radial direction with value $10^{-4} \times B_T$. The influence of RMPs in a various runaway experimental scenarios is being investigated. RMP configuration: $n=1$ (toroidal mode number), coils above and under the midplane with a possible mutual phase shift in the toroidal angle ϕ was used. The experiments with the phase shift $\phi = \pi/2$ are shown in Figure 6.13. The RMPs clearly have some influence on the low-energy RE presence and perhaps cause a confinement reduction during the time they are applied. The black and red signal show effect of RMPs in the thermal plasma. The green and blue signal show effect of RMPs on the formed RE beam after MGI induced disruption. This can be deduced from the shown comparison.

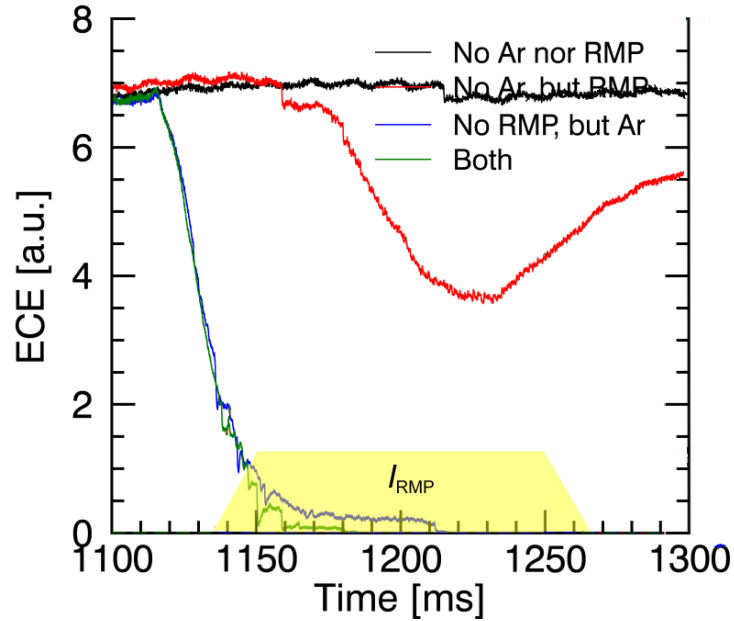


Figure 6.13: V-ECE signal from the RE beam in the discharges with the MGI and RMPs ($\Delta\phi = \pi/2$). Used with permission of T. Markovič. (O,ch1)



Conclusions

This thesis deals with electron cyclotron emission diagnostics of runaway electrons in the COMPASS tokamak. The goal was to utilize the final design of the radiometer for the runaway electron measurements with the help of simulations. This diagnostics uses the vertical view of a plasma along the line of the constant magnetic field and receives the waves with the frequencies 76.5–88.3 GHz. In this setup it is possible to measure low-energy runaway electrons with energies 50–140 keV. The EC wave measurement proved to be useful tool for the runaway electron research and it can be used as a standard diagnostics for the following experiments.

This thesis provides a brief introduction in the problematic of a hot plasma matter, where the principal definitions and important quantities are described. Then the tokamak device is introduced together with its main features, the principle of functioning and most importantly the tokamak topology and the most used coordinate systems.

The current state of art of the runaway electron physics is provided. It focuses on the runaway electron generation mechanisms, mainly on the primary Dreicer mechanism, hot-tail mechanism and avalanche. The methods of the runaway electron measurement are described as well.

The largest part of the theory is dedicated to the waves in plasma. The derivation of the dispersion relations is provided for the basic plasma oscillation, through the electromagnetic waves in a cold magnetised plasma and ends with a brief description of the dispersion relation of the waves in a hot magnetised plasma. In every of these cases the cutoff and resonance conditions are discussed so the reader should have a comprehensive overview of the electromagnetic wave-plasma interaction topic.

The experimental part starts with the description of the COMPASS tokamak and the ECE/EBW radiometer which were used in the measurements of the vertical electron cyclotron emission of the suprathermal electrons. Firstly, it was necessary to properly design the radiometer for the suprathermal electrons measurements. It was decided to use the vertical port and to have view along the constant magnetic field line. With respect to the COMPASS tokamak parameters, especially the low magnetic field and the high electron density in terms of the V-ECE measurement, the E2-band with 76.5–88.3 GHz frequency spectra was chosen. The measurement of these frequencies

should provide direct information of the electrons in 50–570 keV energy spectra. These energies are carried by the low-energy runaway electrons in some dedicated campaigns. The simulations of the optical depth showed the insufficient value of the optical depth. The value was quite low ($\tau < 1$) in the case of the extraordinary mode (X-mode) $\tau \approx 0.1$. It was even lower and in the case of the ordinary mode (O-mode) $\tau \approx 0.005$. This brought us to the situation where the reflected emission can be detected and has to be taken into account in analysis. The detection of the X-mode polarisation and the E2-band with 76.5–88.3 GHz was chosen for the first measurements.

Very important part of the thesis is a confirmation of the source of the emission. By the analysis of the V-ECE signal, no direct dependence on the electron density was found except the cutoff condition. The influence of the thermal emission was also not detected. Although, the reflected waves are detected, what can be deduced from the X-mode and O-mode measurement comparison. The number of the runaway electrons present in the discharge correlates with the V-ECE signal. In the subsequent analysis we can observe consequences of the primary generation. In the density ramp-down scenarios there is a strong correlation between the V-ECE diagnostics of the RE presence and HXR diagnostics of the RE losses. The RE confinement time can be estimated from these experiments. In general, the V-ECE have proven to be highly useful diagnostic method in the terms of the low-energy runaway electron detection. The RE threshold measurements agree with the results obtained on other tokamak devices. The ratio of the electric field and critical field in the RE threshold was analysed and has value $E/E_c \approx 12$. The role of the runaway seed in the low-density scenarios was investigated. The partial results from other RE experiments within the runaway electron dedicated campaign were presented including the massive gas injection and resonant magnetic field experiments.

The V-ECE measurement provides information about the low-energy runaway electron presence especially about the primary generation at the beginning and in the flat-top phase of the discharge. It can be used as a routine diagnostics in the RE campaigns even for other experiments including the runaway electron mitigation scenarios.

The design of the V-ECE diagnostics and performed simulations were presented by the author as a poster presentation at the 20th Joint Workshop on Electron Cyclotron Emission (ECE) and Electron Cyclotron Resonance Heating (ECRH) before the diploma thesis defence. The results obtained by the V-ECE diagnostics in terms of the runaway electron physics will be also presented as a poster presentation at the 45th European Physical Society Conference on Plasma Physics.



Index

- Appelton-Hartree formula, 22
- avalanche mechanism, 13
- bremsstrahlung, 14
- Cherenkov radiation, 14
- collision frequency, 9
- critical electric field, 10
- critical velocity, 11
- current quench, 12
- cutoff frequency, 19
- cyclotron resonant equation, 26
- Debye length, 5
- disruption, 12
- Dreier field, 10
- EBW - el. Bernstein waves, 36
- ECE - el. cyclotron emission, 26
- electron cyclotron frequency, 21
- electron plasma frequency, 18
- fusion, 1
- HFS - high field side, 7
- HXR - hard X-ray, 15
- Kirchhoff's law, 30
- L-mode, 23
- Larmor radius, 5
- LCFS - last closed flux surface, 8
- LFS - low field side, 7
- Maxwell equations, 18
- MGI - massive gas injection, 56
- O-mode, 23
- optical depth, 30
- optical index, 22
- perturbation calculus, 17
- photoneutrons, 15
- R-mode, 23
- radiation transfer, 30
- ray equations, 29
- RMP - resonant magnetic perturbation , 58
- Stix's notation, 22
- synchrotron radiation, 14
- thermal quench, 12
- toroidal magnetic field \mathbf{B}_ϕ , 7
- V-ECE - vertical ECE, 27
- Vlasov equation, 24
- wave vector, 20
- X-mode, 23



Bibliography

- [1] F. F. Chen. *Introduction to Plasma Physics and Controlled Fusion*. Springer International Publishing, Springer, 2016.
- [2] Culham Centre for Fusion Energy web page. *How fusion works?* http://www.ccfе.ac.uk/How_fusion_works.aspx.
- [3] J. Wesson and D. Campbell. *Tokamaks*. Oxford University Press, New York, 2011.
- [4] K. Miyamoto. *Controlled Fusion and Plasma Physics*. Taylor and Francis, New York, 2006.
- [5] C. Abud and I. Caldas. Impact of punctual flat magnetic shear on the field line transport. *Physics of Plasmas*, 22(6):062510, 2015. <http://aip.scitation.org/doi/abs/10.1063/1.4923016>.
- [6] R. Jaspers. *Relativistic Runaway Electrons Tokamak Plasmas*. Technische Universiteit Eindhoven, 1995. http://www.iaea.org/inis/collection/NCLCollectionStore/_Public/27/012/27012481.pdf.
- [7] H. Knoepfel and D. A. Spong. Runaway electrons in toroidal discharges. *Nuclear Fusion*, 19(6):785–829, 1979. <http://iopscience.iop.org/0029-5515/19/6/008>.
- [8] H. Dreicer. Electron and Ion Runaway in a Fully Ionized Gas. I. *Physical Review*, 115(2):238–249, 1959. <https://journals.aps.org/pr/abstract/10.1103/PhysRev.115.238>.
- [9] H. Dreicer. Electron and Ion Runaway in a Fully Ionized Gas. II. *Physical Review*, 117(2):329–342, 1960. <https://journals.aps.org/pr/abstract/10.1103/PhysRev.117.329>.
- [10] R. S. Granetz, B. Esposito, et al. An ITPA joint experiment to study runaway electron generation and suppression. *Physics of Plasmas*, 21(7), 2014. <http://aip.scitation.org/doi/10.1063/1.4886802>.
- [11] O. Ficker. Generation, losses and detection of runaway electrons in tokamaks. Master’s thesis, České vysoké učení technické v Praze, 2017. <http://stacks.iop.org/0029-5515/57/i=7/a=076002>.

- [12] H. M. Smith and E. Verwichte. Hot tail runaway electron generation in tokamak disruptions. *Physics of Plasmas*, 15(7), 2008. <http://aip.scitation.org/doi/10.1063/1.2949692>.
- [13] M. Rosenbluth and S. Putvinski. Theory for Avalanche of Runaway Electrons in Tokamaks. *Nuclear Fusion*, 37(10):1689–1699, 1997. <http://iopscience.iop.org/0029-5515/37/10/I03>.
- [14] E. Mazzucato. *Electromagnetic waves for thermonuclear fusion research*. World Scientific, Singapore, 2014.
- [15] P. Kulhánek. *Úvod do teorie plazmatu*. Aldebaran Group for Astrophysics, Prague, 2017.
- [16] T. H. Stix. *Waves in Plasma*. American Institute of Physics, New York, 1992.
- [17] D. G. Swanson. *Series in Plasma Physics Plasma Waves*. IOP, Philadelphia, 2003.
- [18] J. Urban. *Electron Bernstein Wave Emission Simulations for Spherical Tokamaks*. PhD thesis, České vysoké učení technické v Praze, 2008. http://server.ipp.cas.cz/~urban/Dissertation_JU.pdf.
- [19] V. D. Shafranov. *Reviews of Plasma Physics*. Vol. 3. Consultants Bureau, New York-London, 1967.
- [20] M. Bornatici, O. De Barbieri, and F. Engelmann. Electron Cyclotron Emission and Absorption in Fusion Plasmas. *Nuclear Fusion*, 23(9):1153–1257, 1983. <http://iopscience.iop.org/article/10.1088/0029-5515/23/9/005/pdf>.
- [21] I. H. Hutchinson. *Principles of Plasma Diagnostics*. Cambridge University Press, New York, 2002. <http://iopscience.iop.org/article/10.1088/0741-3335/44/12/701/meta>.
- [22] G. Taylor et al. Status of the design of the ITER ECE diagnostic. *EPJ Web of Conferences*, 87:03002, 2015. <https://doi.org/10.1051/epjconf/20158703002>.
- [23] D. R. Roberts, R. F. Steimle, et al. Vertical viewing of electron-cyclotron emissions for diagnosing fast-electron dynamics in TEXT-U. *Review of Scientific Instruments*, 66(57):427–429, 1995. <http://scitation.aip.org/content/aip/journal/rsi/66/1?ver=pdfcov>.
- [24] F. J. Stauffer, D. A. Boyd, et al. TFTR Michelson interferometer electron cyclotron emission diagnostic. *Review of Scientific Instruments*, 56(5):925–927, 1985. <http://aip.scitation.org/doi/10.1063/1.1138044>.

- [25] P. Blanchard, S. Alberti, et al. High field side measurements of non-thermal electron cyclotron emission on TCV plasmas with ECH and ECCD. *Plasma Phys. Control. Fusion*, 44(4402):2231–2249, 2002. <http://iopscience.iop.org/0741-3335/44/10/310>.
- [26] J. Reed, S. Janz, R. Ellis, and John Lohr. Electron density measurements from cutoff of electron cyclotron emission in the DIII-D tokamak. *Review of Scientific Instruments*, 59(8):1608–1610, 1988. <http://aip.scitation.org/doi/10.1063/1.1140162>.
- [27] D. Farina, L. Figini, P. Platania, and C. Sozzi. SPECE: A code for electron cyclotron emission in tokamaks. In *AIP Conference Proceedings*, volume 988, pages 128–131, 2008. <http://aip.scitation.org/doi/abs/10.1063/1.2905053>.
- [28] IPP of the CAS web page. *COMPASS tokamak*. http://www.ipp.cas.cz/vedecka_struktura_ufp/tokamak/tokamak_compass/.
- [29] J. Zajac, J. Preinhaelter, J. Urban, et al. EBE/ECE Radiometry on COMPASS Tokamak—Design and First Measurements. In *AIP Conference Proceedings*, volume 1187, pages 473–476, 2009. <http://proceedings.aip.org/proceedings/confproceed/1187.jsp>.
- [30] J. Zajac, J. Preinhaelter, J Urban, et al. Electron cyclotron-electron Bernstein wave emission diagnostics for the COMPASS tokamak. *Review of Scientific Instruments*, 81(10), 2010. <http://aip.scitation.org/doi/10.1063/1.3475715>.
- [31] O. Ficker et al. Losses of runaway electrons in MHD-active plasmas of the COMPASS tokamak. *Nuclear Fusion*, 57(7):076002, 2017. <http://aip.scitation.org/doi/10.1063/1.4886802>.
- [32] Vlainic et al. Post-disruptive runaway electron beams in the compass tokamak. *Journal of Plasma Physics*, 81(5):475810506, 2015.
- [33] K. Kato and I. H. Hutchinson. Alcator C vertical viewing electron cyclotron emission diagnostic. *Review of Scientific Instruments*, 57(8):1959–1961, 1986. <http://aip.scitation.org/doi/abs/10.1063/1.1138806>.
- [34] K. Kato and I. H. Hutchinson. Nonthermal electron velocity distribution measured by electron cyclotron emission in Alcator C tokamak. *Physical Review Letters*, 56(4):340–343, 1986. <https://journals.aps.org/prl/abstract/10.1103/PhysRevLett.56.340>.
- [35] H. J. Hartfuss, T. Geist, and M. Hirsch. Heterodyne methods in millimetre wave plasma diagnostics with applications to ECE, interferometry and reflectometry. *Plasma Phys. Control. Fusion*, 39:1693–1769, 1997. <http://iopscience.iop.org/article/10.1088/0741-3335/39/11/001/meta>.